Journal of Fluids and Structures 73 (2017) 100–124

Contents lists available at ScienceDirect

Journal of Fluids and Structures

journal homepage: www.elsevier.com/locate/jfs

Extension of the Non-Linear Harmonic method for the study of the dynamic aeroelasticity of horizontal axis wind turbines

Sergio González Horcas [a,b,*], François Debrabandere [a], Benoît Tartinville [a], Charles Hirsch [a], Grégory Coussement [b]

[a] NUMECA International, 189 Ch. de la Hulpe, B-1170 Bruxelles, Belgium
[b] University of Mons, Faculty of Engineering, Fluids-Machines Unit, 53 Rue du Joncquois, B-7000 Mons, Belgium

HIGHLIGHTS

- The paper presents an innovative approach for dynamic aeroelasticity simulation.
- It couples the Non-Linear Harmonic method with a linearized structural model.
- The method is first applied to a cylinder undergoing vortex induced vibrations.
- A complete horizontal axis wind turbine is also studied, including the tower.
- Promising results are obtained, with a very good computational efficiency.

ARTICLE INFO

Article history:
Received 23 October 2016
Received in revised form 4 May 2017
Accepted 12 June 2017
Available online 22 June 2017

Keywords:
Aeroelasticity
Computational Fluid Dynamics
DTU 10MW RWT
Fluid–Structure Interaction
Horizontal axis wind turbine
Non-Linear Harmonic

ABSTRACT

In this paper an innovative methodology for the study of horizontal axis wind turbines dynamic aeroelasticity is presented. It can be understood as an extension of the *Non-Linear Harmonic* (NLH) method, an efficient computational approach for the analysis of unsteady periodic flows. A linearized model of the structure consisting of a set of mode shapes and natural frequencies was included. The aeroelastic equilibrium was ensured through a set of equations linking the structural displacements and the fluid loads for both the time-averaged and the harmonic contributions. First, the developed methodology is tested in the framework of a 2D cylinder mounted on a single degree of freedom elastic system and undergoing *Vortex Induced Vibrations* (VIV). The results are compared with previous experimental and computational studies, revealing the potential of the method for the prediction of both the shedding frequency and the aeroelastic response. Secondly, the dynamic aeroelasticity of the complete DTU 10MW RWT wind turbine (i.e. including the tower) is assessed. A nominal operating point is studied, and the rotor flexibility is considered via a blade structural model. The results of this *Fluid–Structure Interaction* (FSI) simulation are compared with two additional computations, both assuming *rigid* blades, that modeled the isolated DTU 10MW RWT rotor and the complete machine. This allowed to distinguish the impact of the blade flexibility on the rotor performance from the potential effects associated to the presence of the tower. In particular, the consideration of the aeroelasticity led to a decrease of the predicted time-averaged rotor loads and the corresponding amplitudes of oscillation. For its application on the DTU 10MW RWT, the developed methodology was found to be one order of magnitude faster than a standard time marching approach.

* Corresponding author at: NUMECA International, 189 Ch. de la Hulpe, B-1170 Bruxelles, Belgium.
E-mail address: sergio.horcas@gmail.com (S.G. Horcas).

http://dx.doi.org/10.1016/j.jfluidstructs.2017.06.008
0889-9746/

Nomenclature

Latin letters

$\mathbf{C}$	Generalized damping matrix
C_D	Drag coefficient
C_L	Lift coefficient
D	Diameter
d_n	Deformation normal to rotor axis
d_p	Deformation parallel to rotor axis
D_y	Cylinder displacement
F	Force
$\vec{F}_I$	Vector of inviscid fluxes
f_k	Spring frequency
f_{rot}	Rotor frequency
$\vec{f}_S$	Fluid load
f_{shed}	Shedding frequency
f_{shnat}	Natural shedding frequency
$\vec{F}_V$	Vector of viscous fluxes
$\vec{g}$	Heat flux
H	Total enthalpy
$\mathbf{I}$	Unit tensor
I	Imaginary number
k^*_{eff}	Effective stiffness
L	Span
m	Mass
p	Pressure
$\vec{q}$	Vector of generalized displacements
Q	Vector of source terms
q	Generalized displacement
R	Blade radius
r	Radial position
Re	Reynolds number
$\vec{S}$	Surface vector
St	Strouhal number
St_{shnat}	Natural Strouhal number
T	Rotation period
t	Time
$\vec{u}$	Deformation vector
U	Vector of conservative flow variables
U_∞	Freestream velocity
$\vec{v}$	Velocity vector

Greek letters

θ	Azimuth angle
ρ	Density
$\boldsymbol{\tau}$	Stress tensor
$\boldsymbol{\phi}$	Eigenvectors matrix
ξ	Damping ratio
ω	Angular velocity/Natural frequency
Ω	Volume
$\Delta\alpha$	Phase change per iteration

Subscripts

Im	Imaginary part
Re	Real part

Superscripts

$\bar{}$	Time-averaged
$'$	Fluctuation

$''$	Perturbation
T	Transpose
$\tilde{}$	Harmonic complex amplitude

Acronyms

BEM	Blade Element Momentum
BPF	Blade Passing Frequency
CFD	Computational Fluid Dynamics
FEM	Finite Element Method
FSI	Fluid–Structure Interaction
HAWT	Horizontal Axis Wind Turbine
IDW	Inverse Distance Weighting
NLH	Non-Linear Harmonic
RANS	Reynolds-Averaged Navier–Stokes
RBF	Radial Basis Function
RMS	Root Mean Square
RPM	Revolutions Per Minute
TFI	Transfinite Interpolation
URANS	Unsteady Reynolds-Averaged Navier–Stokes
VIV	Vortex Induced Vibrations

1. Introduction

Industry standards for the aerodynamic simulations of *Horizontal Axis Wind Turbines* (HAWTs) are based on the *Blade Element Momentum* (BEM) theory (Glauert, 1935). Such a method offers a very good computational efficiency for an acceptable blade loading estimation. The accuracy of the BEM approach is however limited due to the existence of highly skewed 3D flows and heavy flow detachments. This motivates the use of high fidelity flow modeling methods based on the 3D solution of the Navier–Stokes equations as a complementary design tool. These techniques are often simply referred to as *Computational Fluid Dynamics* (CFD) methods. Traditional CFD applications to HAWTs analysis are based on steady flow simulations of the isolated rotor and under the hypothesis of *rigid* blades (Aranake, 2013; Yelmule and Anjuri, 2013; Suárez and Doerffer, 2015). Thanks to the problem periodicity when assuming an uniform upstream wind aligned with the rotor axis, a single blade passage can be considered. These isolated rotor simulations allow to characterize the local flow behavior around the wind turbine and its impact on the global performance with a reduced computational effort. However, by omitting the tower geometry, one of the main sources of flow unsteadiness is also neglected. Indeed, the proximity of the HAWT rotor to the tower introduces an azimuthal dependency on the flow solution, with expected blade loading decays at every *blade–tower alignment*. In addition, when considering the full machine this time varying loading can lead to significant blade deformations during operation, due to dynamic aeroelasticity phenomena. This requires the modeling of the so-called *Fluid–Structure Interaction* (FSI) in the used numerical approach. In particular, the mutual interaction between the blade deflections and the fluid loading should be assessed by a *2-way coupling* FSI strategy.

Several authors performed FSI simulations of a complete HAWT (i.e. including the tower) by coupling high fidelity CFD methods with structural models. Carrión (2014) analyzed the aeroelastic response of the NREL Phase VI for different operating points. The rotor radius R of this HAWT is 5 m, and it accounts for 2 blades. An *Unsteady Reynolds-Averaged Navier–Stokes* (URANS) flow solver was employed, together with a modal representation of the blade structure. At rated speed, time-averaged blade tip deflections parallel to the rotor axis of 0.25%R were predicted, with maximum oscillations of 0.013%R. A more important role of the aeroelasticity was observed in the studies of the 3-bladed NREL 5 MW, with $R = 63$ m. Hsu and Bazilevs (2012) predicted time-averaged blade tip deformations of 2.5%R, with amplitudes of oscillation of approximately 0.4%R. The adopted computational approach was a combination of the variational multi-scale formulation of the Navier–Stokes equations and a blade structural model, based on isogeometric analysis. Similar deflections were found in the subsequent work of Yu and Kwon (2014), where a precone angle of 2.5°was also considered in the assembly. A URANS solver was employed, together with a beam-based blade model. The comparison of the simulations with and without the consideration of the FSI allowed to estimate the effect of the dynamic aeroelasticity on the overall rotor performance. The authors attributed to this phenomenon a reduction of the time-averaged thrust of 11%, while the time-averaged power was decreased by 6%. In addition an attenuation of the main harmonic of the rotor loads was observed, with approximate reductions of 33% for the thrust and 43% for the power. The recent work of Heinz et al. (2016) also showed a very good agreement with the previous reference. Furthermore, the authors presented a comparison of the performance of BEM and URANS flow models. Both approaches predicted similar results for the studied load cases, with small differences in the computed blade loading at low and high span ranges. The three-dimensionality of the flow near the blade root and the blade tip was pointed out as a feasible cause for these discrepancies.

All the aforementioned simulations followed a time marching strategy for the solution of the flow and the aeroelastic equations. Due to their associated computational time when studying HAWT rotor aerodynamics, the industrial application of these methods is still limited to particular load cases and configurations. An alternative and less costly methodology is explored in this paper. In particular the *Non-linear Harmonic* (NLH) approach, introduced by He and Ning (1998) and industrialized by Vilmin et al. (2006), was extended in order to perform dynamic aeroelasticity studies of HAWTs. This required the implementation of a *2-way coupling* FSI methodology formulated in the harmonic domain, both for the flow equations and the periodic unsteady deformation of the CFD mesh induced by the deflection of the geometry. To the best of the authors' knowledge, this paper constitutes the first experience of introducing such an approach in a NLH solver. Similar works were previously performed in the framework of the also non-linear frequency method referred to as the *Harmonic Balance* (Hall et al., 2002). To this group belong the works of Dowell et al. (2008) and Besem (2015) about the *Vortex Induced Vibrations* (VIV) of cylinders, the F-16 fighter studies of Thomas et al. (2004, 2005), and the elastically mounted airfoil analysis included in Thomas et al. (2002) and Liu et al. (2005). The application of non-linear frequency methods to wind energy applications has mainly focused in the study of representative HAWTs airfoils by means of 2D simulations. Of particular interest are the works of Campobasso et al. (2014b, a) with the *Harmonic Balance* method. A similar methodology was followed in Howison and Ekici (2014), where a pitching wind turbine airfoil was studied. In a recent publication, the same author studied the flutter of a wind turbine blade accounting for a radius of 35 m (Howison, 2015). This was performed by a *1-way coupling* FSI approach. The effect of each of the structural modes was independently assessed by imposing a small amplitude harmonic motion and analyzing the resulting aerodynamic loading on the blade.

The *2-way coupling* FSI methodology developed in the present publication was used to study the dynamic aeroelasticity of the DTU 10 MW RWT (Bak et al., 2013) at nominal operation. This HAWT has a 3-bladed rotor with $R = 89.166$ m. The present work can be seen as a continuation of the NLH computations of the DTU 10 MW RWT full machine presented in Horcas et al. (2016b), where the performance and the potential of the harmonic solution were discussed. Contrary to the aforementioned publication, in this paper the flexibility of the rotor is taken into account by introducing a structural model of the blades. In order to assess the performance of the proposed approach in a simpler case prior to its application in a complete HAWT, the study of a non-rotating 2D geometry was considered. An alternative source of flow unsteadiness was then required for the application of the NLH method, rather than the *rotor/stator* or *rotor/rotor* interactions. In this context, the so-called *vortex shedding* phenomenon was selected. In particular, a test case consisting of a cylinder mounted on a single degree of freedom elastic system which is excited by its laminar vortex shedding was analyzed. This oscillation mechanism can be classified into the group of VIV phenomena.

2. Methods

The proposed methodology was implemented in the commercial CFD package FINE^{TM}/Turbo (NUMECA International, 2016b). The FINE^{TM}/Turbo solver is a three-dimensional, density-based, structured, multi-block finite volume code. The discretization in space is based on a cell centered control volume approach. Both upwind schemes and central schemes are available. The latter method was used in this paper, in combination with Jameson type artificial dissipation (Jameson et al., 1981). A four-stage explicit Runge–Kutta scheme is applied for the temporal discretization. Multi-grid method, local time-stepping and implicit residual smoothing are used in order to speed-up the convergence for steady computations. For unsteady simulations, both dual time-stepping or NLH methods are available. Regarding HAWT applications, FINE^{TM}/Turbo was previously validated in the framework of NREL Phase VI isolated rotor simulations (Fan and Kang, 2009; Elfarra et al., 2014; Suárez et al., 2015).

2.1. Description of the NLH method

In the NLH approach, the instantaneous conservative flow variables $U = \left(\rho, \rho v_x, \rho v_y, \rho v_z, \rho E\right)$ are decomposed into a time-averaged value $\bar{U}$ and a sum of unsteady perturbations U_n'', assumed to be periodic in time:

$$U\left(\vec{x}, t\right) = \bar{U}\left(\vec{x}\right) + \sum_n U_n''\left(\vec{x}, t\right), \tag{1}$$

A Fourier decomposition is applied to each of the periodic perturbations. Hence, the perturbation U_n'' can be written as a finite sum of N_h time harmonics:

$$U_n''\left(\vec{x}, t\right) = \sum_{h=1}^{N_h}\left[\tilde{U}|_h\left(\vec{x}\right)e^{I\omega_h t} + \tilde{U}|_{-h}\left(\vec{x}\right)e^{-I\omega_h t}\right] = 2\sum_{h=1}^{N_h}\left[\tilde{U}^h_{Re}cos\left(\omega_h t\right) - \tilde{U}^h_{Im}sin\left(\omega_h t\right)\right], \tag{2}$$

where the harmonic amplitudes $\tilde{U}|_h$ and $\tilde{U}|_{-h}$ are complex conjugates related to the nth perturbation and are defined by the real part $\tilde{U}^h_{Re}$ and the imaginary part $\tilde{U}^h_{Im}$.

The value of N_h is understood as an input of the method and it drives the spatial and frequency resolution of the computed flow unsteadiness. For the particular case of rotating machinery applications and due to the relative motion of the different stages, the *Blade Passing Frequencies* (BPFs) of each bladerow correspond to the fundamental harmonic frequencies ω_1 that

Table 1
Considered fundamental harmonic frequencies for two consecutive bladerows a and b in the scope of a turbomachinery application. All the superscripts included in this table refer to this distinction.

	Bladerow a	Bladerow b
Rotational speed	R^a	R^b
Number of blades	M^a	M^b
Blade passing frequency	$P^a = M^a \left\|R^a - R^b\right\|$	$P^b = M^b \left\|R^a - R^b\right\|$
Fundamental harmonic frequency due to adjacent bladerow	$\omega_1^a = P^b$	$\omega_1^b = P^a$

they provide to the adjacent bladerows. This is exemplified in Table 1 for the particular case of two consecutive bladerows a and b.

The NLH formulation can be derived by introducing the variable decomposition of Eq. (1) into the unsteady Reynolds-Averaged Navier–Stokes equations. A new set of equations in the frequency domain is then obtained, associated to the time-mean contribution of every conservation law and the corresponding harmonics. Using a compact finite-volume formulation, they can be written as:

$$\sum_{\text{cellfaces}} \left(\overline{\vec{F}_I} - \overline{\vec{F}_V}\right) \cdot \vec{S} = \bar{Q}\,\Omega, \tag{3}$$

$$I\omega_h \widetilde{U}|_h \Omega + \sum_{\text{cellfaces}} \widetilde{\vec{F}}_I|_h \cdot \vec{S} - \sum_{\text{cellfaces}} \widetilde{\vec{F}}_V|_h \cdot \vec{S} = \widetilde{Q}|_h \Omega, \tag{4}$$

with:

$$\overline{\vec{F}_I} \cdot \vec{S} = \begin{pmatrix} \overline{\rho \vec{v}} \vec{S} \\ \overline{\rho \vec{v} v_x} \vec{S} + \bar{p} S_x \\ \overline{\rho \vec{v} v_y} \vec{S} + \bar{p} S_y \\ \overline{\rho \vec{v} v_z} \vec{S} + \bar{p} S_z \\ \overline{\rho H \vec{v}} \vec{S} \end{pmatrix} + \begin{pmatrix} 0 \\ \overline{(\rho \vec{v})'' v_x''} \vec{S} \\ \overline{(\rho \vec{v})'' v_y''} \vec{S} \\ \overline{(\rho \vec{v})'' v_z''} \vec{S} \\ \overline{(\rho H)'' \vec{v}''} \vec{S} \end{pmatrix}; \qquad \overline{\vec{F}_V} \cdot \vec{S} = \begin{pmatrix} 0 \\ \overline{\tau_{xx}} S_x + \overline{\tau_{xy}} S_y + \overline{\tau_{xz}} S_z \\ \overline{\tau_{xy}} S_x + \overline{\tau_{yy}} S_y + \overline{\tau_{yz}} S_z \\ \overline{\tau_{xz}} S_x + \overline{\tau_{yz}} S_y + \overline{\tau_{zz}} S_z \\ \bar{\boldsymbol{\tau}} \bar{\vec{v}} \vec{S} + \bar{\vec{g}} \vec{S} \end{pmatrix} + \begin{pmatrix} 0 \\ 0 \\ 0 \\ 0 \\ \overline{\boldsymbol{\tau}'' \vec{v}''} \vec{S} \end{pmatrix}$$

$$\widetilde{\vec{F}}_I|_h \cdot \vec{S} = \begin{pmatrix} \widetilde{\rho \vec{v}}|_h \vec{S} \\ \overline{\rho \vec{v}} \widetilde{v_x}|_h \vec{S} + \widetilde{\rho \vec{v}}|_h \overline{v_x} \vec{S} + \tilde{p}|_h S_x \\ \overline{\rho \vec{v}} \widetilde{v_y}|_h \vec{S} + \widetilde{\rho \vec{v}}|_h \overline{v_y} \vec{S} + \tilde{p}|_h S_y \\ \overline{\rho \vec{v}} \widetilde{v_z}|_h \vec{S} + \widetilde{\rho \vec{v}}|_h \overline{v_z} \vec{S} + \tilde{p}|_h S_z \\ \widetilde{\rho H}|_h \bar{\vec{v}} \vec{S} + \overline{\rho H} \widetilde{\vec{v}}|_h \vec{S} \end{pmatrix}; \qquad \widetilde{\vec{F}}_V|_h \cdot \vec{S} = \begin{pmatrix} 0 \\ \widetilde{\tau_{xx}}|_h S_x + \widetilde{\tau_{xy}}|_h S_y + \widetilde{\tau_{xz}}|_h S_z \\ \widetilde{\tau_{xy}}|_h S_x + \widetilde{\tau_{yy}}|_h S_y + \widetilde{\tau_{yz}}|_h S_z \\ \widetilde{\tau_{xz}}|_h S_x + \widetilde{\tau_{yz}}|_h S_y + \widetilde{\tau_{zz}}|_h S_z \\ \bar{\boldsymbol{\tau}} \widetilde{\vec{v}}|_h \vec{S} + \widetilde{\boldsymbol{\tau}}|_h \bar{\vec{v}} \vec{S} + \widetilde{\vec{g}}|_h \vec{S} \end{pmatrix} \tag{5}$$

where $\vec{F}_I$ and $\vec{F}_V$ are the vectors containing the inviscid and viscous terms, respectively. The vector Q refers to the source terms (including Coriolis and centrifugal terms in rotatory problems), and the complex contribution $I\omega_h \widetilde{U}|_h \Omega$ was induced by the casting in the frequency domain. The second terms of $\overline{\vec{F}_I} \cdot \vec{S}$ and $\overline{\vec{F}_V} \cdot \vec{S}$ expressions of Eq. (5) correspond to the *deterministic stresses*. These are present due to the non-linearity of the formulation, as the *Reynolds stresses* appear in the derivation of the *Reynolds-Averaged Navier–Stokes* (RANS) equations. The role of the *deterministic stresses* is then to account for the contribution of the flow unsteadiness into the time-mean flow equations, and they are directly calculated from the in-phase and out-of-phase components of the solved harmonics. Being the starting point of the NLH method derivation the *Reynolds-Averaged Navier–Stokes* equations, both the heat flux $\vec{g}$ and the stress tensor $\boldsymbol{\tau}$ contain stresses related to the turbulent effects that need of a closure model. In the NLH approach implemented in FINE™/Turbo solver, this task is carried out by means of a linear eddy viscosity turbulence model. Both the laminar and eddy viscosities are computed based on the time-mean flow variables, assuming that they are unaffected by the unsteady fluctuations.

As for the RANS approach, the obtained formulation is only space-dependent. The solution of the system is performed by time-marching to a steady-state solution the time-mean and harmonic flow equations. This is achieved by introducing pseudo-time derivatives in Eqs. (3) and (4), that are driven to zero during the simulation. The transformation from time-dependent equations into steady ones justifies the computational time saving attributed to the NLH approach. In addition the NLH methodology applied to rotating machinery problems only requires the meshing of a single blade passage, while unsteady time marching computations usually need the full rotor and stator meshing. Even if the flow variables are solved in the frequency domain, the results of a NLH method simulation can be easily reconstructed in time in order to perform a more comprehensive post-processing of the unsteady periodic flow. This process is referred to in this document as *time reconstruction*. The NLH belongs to a family of techniques often referred as non-linear frequency methods. Other examples of these approaches are the *Harmonic Balance* (Hall et al., 2002) and the *Non-Linear Frequency Domain* (McMullen,

2003). Contrary to the two aforementioned techniques, in the NLH approach the Navier–Stokes equations are completely formulated and solved in the frequency domain, including the viscous terms and the turbulence model.

2.2. Extension of the NLH method for 2-way coupling FSI simulations

To introduce the aeroelastic equilibrium in the FINE™/Turbo solver, the linearized aeroelastic equation relating the fluid loads $\vec{f}_S$ and the vector of structural generalized displacements $\vec{q}$ was considered:

$$\mathbf{I}\frac{\partial^2\vec{q}}{\partial t^2} + \mathbf{C}\frac{\partial\vec{q}}{\partial t} + \mathbf{diag}\left[\omega_k^2\right]\vec{q} = \boldsymbol{\phi}^T\vec{f}_S \tag{6}$$

where $\mathbf{C}$ is the generalized damping matrix, $\boldsymbol{\phi}$ is the eigenvectors matrix (normalized by the mass) and ω_k the eigenfrequency corresponding to the mode k.

For rotatory applications the fluid vector $\vec{f}_S$ also accounted for the centrifugal loads, but the effects of gravity were neglected in the current implementation. The consideration of gravity would lead in an additional time-varying load in the blades, mainly acting in the in-plane direction and synchronized with the frequency of rotation. Eq. (6) was further simplified, following the modal damping approach, by assuming a diagonal generalized damping matrix. This allowed to uncouple the equations for every mode, making their resolution easier and computationally more efficient. In particular Adhikari (2000) found that, for large systems, this diagonalization approximation was one order of magnitude faster than other solution methods, involving a transformation to the state space and the use of complex mode shapes and frequencies. It should be remarked that, for rotor dynamics applications, the matrix $\mathbf{C}$ can account for the structural damping and the Coriolis contributions. The latter effect, that will introduce off-diagonal terms in the damping matrix, was neglected in the present work. Previous wind turbine studies involving the use of CFD solvers followed the same hypothesis (Corson et al., 2012; Carrión, 2014), or completely disregarded the effects of damping (Howison et al., 2015). The non consideration of the Coriolis effects limits the application of the method for the study of flutter and instabilities, since the induced coupling between the different mode shapes was found to be very important in the prediction of these phenomena for HAWTs (Holierhoek, 2008; Velazquez and Swartz, 2012; Owens et al., 2013). Considering a diagonal generalized damping matrix in the form $\mathbf{C_g} = \mathbf{diag}\,[2\xi_k\omega_k]$, the uncoupled system of Eq. (6) reads, for every mode k:

$$\frac{\partial^2 q_k}{\partial t^2} + 2\xi_k\omega_k\frac{\partial q_k}{\partial t} + \omega_k^2 q_k = \vec{\phi}_k^T\vec{f}_S \tag{7}$$

where ξ_k is the damping ratio of the considered mode and $\vec{\phi}_k$ the associated eigenvector, that is often referred to as the structure mode shape.

In order to obtain a formulation of the Eq. (7) adapted to the NLH solver, both the generalized displacements and the fluid loads were decomposed into the corresponding time-averaged and perturbation components:

$$q_k\left(\vec{x},t\right) = \overline{q_k}\left(\vec{x}\right) + \sum_n q''_{k,n}\left(\vec{x},t\right), \tag{8}$$

$$\vec{f}_S\left(\vec{x},t\right) = \overline{\vec{f}}_S\left(\vec{x}\right) + \sum_n \vec{f}''_{S,n}\left(\vec{x},t\right). \tag{9}$$

Introducing the decomposition of Eqs. (8) and (9) into the aeroelastic equilibrium relation of Eq. (7):

$$\frac{\partial^2 q''_k}{\partial t^2} + 2\xi_k\omega_k\frac{\partial q''_k}{\partial t} + \omega_k^2\overline{q_k} + \omega_k^2 q''_k = \vec{\phi}_k^T\overline{\vec{f}_S} + \vec{\phi}_k^T\vec{f}_S{}'' \tag{10}$$

where the set of perturbations of the decomposed quantities were denoted as $\vec{f}_S{}''$ and q''_k for the sake of simplicity.

The time-mean equation of the mode k can be derived by time-averaging Eq. (10):

$$\overline{q_k} = \frac{\vec{\phi}_k^T\overline{\vec{f}_S}}{\omega_k^2}. \tag{11}$$

By casting Eq. (10) into the frequency domain, the resulting aeroelastic equilibrium equation for the hth harmonic becomes:

$$\widetilde{q_k}|_h = \frac{\vec{\phi}_k^T\widetilde{\vec{f}_S}|_h}{\omega_k^2 - \omega_h^2 + 2I\xi_k\omega_k\omega_h}. \tag{12}$$

In order to define the linearized behavior of the structure, the set of values of ω_k, ξ_k and $\vec{\phi}_k$ should be computed prior to the FSI simulation. This information can be obtained either by means of experimental results or by a modal analysis simulation performed with a computational structural mechanics solver. Since the points containing the mode shapes information do not necessarily correspond to the position of the CFD mesh nodes, an additional interpolation step based on the *Radial Basis Function* (RBF) is also performed before the FSI computation.

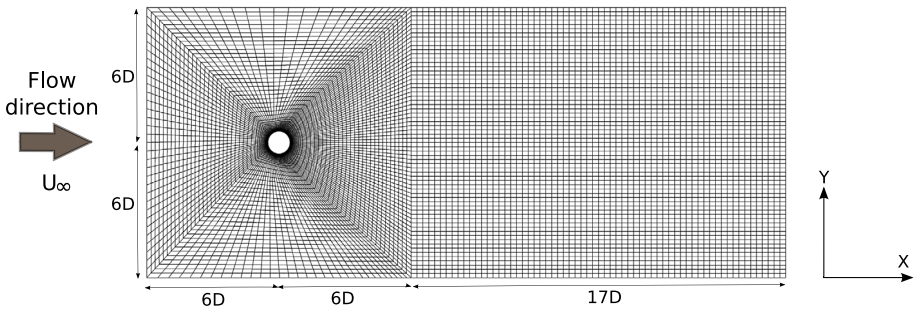

Fig. 1. Cylinder mesh, D refers to the cylinder diameter.

The solid boundaries deformation of the structure $\vec{u}$ can be directly computed with the values of $\overline{q_k}$ and $\widetilde{q_k}$ as:

$$\bar{\vec{u}} = \sum_{k=1}^{N_k} \overline{q_k}\vec{\phi}_k \tag{13}$$

$$\widetilde{\vec{u}}|_h = \sum_{k=1}^{N_k} \widetilde{q_k}|_h\vec{\phi}_k \tag{14}$$

where N_k is the number of considered structure modes.

In order to diffuse the solid boundaries displacement into the whole CFD grid, different mesh deformation methods are implemented in the solver. In particular, this process can be carried out by harmonic extensions of the RBF approach (Debrabandere, 2014), a hybrid method combining the RBF and the *Transfinite Interpolation* (TFI) and denoted in this paper as RBF+TFI (Horcas et al., 2015), and a version of the *Inverse Distance Weighting* (IDW) described in Uyttersprot (2014).

3. Academic application: study of the VIV of a cylinder

A 2D cylinder with a diameter of D was considered, assuming an arbitrary span of L for the loads computation. A mesh accounting for a total of 28,340 nodes and based on an OH topology was used (see Fig. 1). This grid was reproduced from the work of Hakimi (1997), where the vortex shedding at Re = 75 was studied. A first cell height of $10^{-4}D$ was imposed around the cylinder wall. The compressible laminar formulation of the Navier–Stokes equations was adopted for all the presented simulations. A subsonic regime was assumed, with maximum observed *Mach numbers* of approximately 0.5 and an inlet *Mach number* of 0.38 for the studied flow conditions. The fluid was considered to be thermodynamically perfect.

In order to assess the performance of the NLH method when dealing with the identification of the shedding frequency, first simulations were considering a fixed cylinder. The VIV phenomenon was then studied by attaching the cylinder to an elastic mounting, allowing it to oscillate in the transverse direction with respect to the incoming flow.

3.1. Results for the fixed cylinder configuration

The performance of the NLH method when dealing with laminar vortex shedding modeling was assessed by studying different *Reynolds numbers Re* in the range [75; 150]. The solved frequency (i.e. the solved *Strouhal number St*) was imposed prior to the run of the computation, as it is depicted in Fig. 2. In opposition to rotating machinery applications, where the flow unsteadiness can be related to the BPF, the frequency of the *Von Kármán* street could not be pre-computed for this test case. In order to solve this issue, an iterative shedding frequency identification strategy known as the *phase error method* was used. This technique was initially developed by Spiker et al. (2006) when applying the *Harmonic balance* method to the same test case, and subsequently used for similar purposes in Spiker et al. (2009) and Besem (2015). In the *phase error method* two initial simulations are launched, which main harmonics are chosen based on an estimated *St* for the considered flow conditions. The analysis of the converged results of these computations allows to propose a new *St* value, closer to the shedding frequency of the numerical model. This recomputed *St* is used in a subsequent harmonic simulation, and the process continues till a convergence criterion is satisfied.

Let consider the results of a $Re = 75$ simulation accounting for a single harmonic and with a solved *Strouhal number* of 0.139, determined based on an a priori estimation. An undamped periodic oscillatory behavior of the harmonic lift acting on the cylinder was observed during the NLH solver iterations (see Fig. 3). Based on the observations of Spiker et al. (2006), this fact revealed that the solved frequency did not correspond to the natural shedding frequency f_{shnat} for these flow conditions.

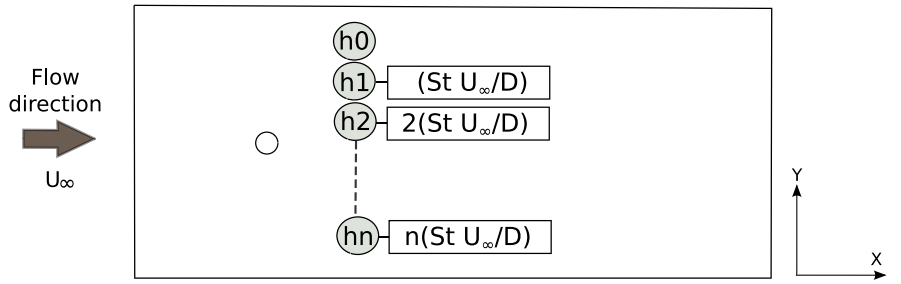

Fig. 2. Diagram of the harmonics involved in a cylinder computation accounting for a total of *n* harmonics. Gray circles contain the harmonic index *hx*, where *h*0 stands for the time mean. Square boxes indicate the frequency attached to every harmonic. These were determined based on the Strouhal number of the fundamental harmonic *St*, that was understood as an input for the solver.

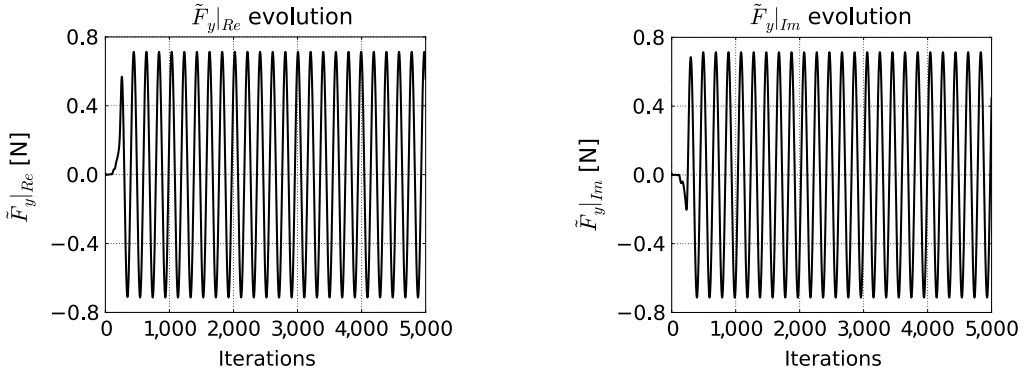

(a) Real part. (b) Imaginary part.

Fig. 3. Fixed cylinder, harmonic lift vs. solver iterations. Simulation at $Re = 75$ and for a solved *St* of 0.139.

The *phase change per iteration* $\Delta\alpha$ of a harmonic quantity $\tilde{A}$ can be defined at this point as the phase difference between two subsequent NLH solver iterations i and $i-1$:

$$\Delta\alpha(\tilde{A})|_i = \alpha(\tilde{A})|_i - \alpha(\tilde{A})|_{i-1}, \tag{15}$$

$$\alpha(\tilde{A}) = \text{atan}\left(\frac{\tilde{A}_{Im}}{\tilde{A}_{Re}}\right), \tag{16}$$

where *Re* and *Im* refer to the real and the imaginary parts of the harmonic quantity, respectively.

The $\Delta\alpha$ operator applied to the harmonic of the cylinder lift force, $\Delta\alpha(\widetilde{F_y})$, was found to be stable after approximately 300 iterations for all the performed computations. This fact is graphically exemplified in Fig. 4. As for the *Harmonic Balance* approach, the stabilized $\Delta\alpha(\widetilde{F_y})$ values showed a quasi-linear dependence with respect to the solved *St*. This allowed to identify the *natural Strouhal number* St_{shnat}, defined here as Df_{shnat}/U_∞, by an iterative minimization process. The value of $|\Delta\alpha(\widetilde{F_y})|$ was considered as converged when a value lower than 0.1° was found. For the final simulation, corresponding to St_{shnat}, the oscillation of the harmonic lift force observed in Fig. 3 vanished. The numerical stability of this final computation could be equivalently observed during the simulation, since the residuals of the harmonics showed faster decay slopes. This remark is in accordance with the application of the *phase error* methodology in the *Harmonic balance* performed by Besem (2015). This *phase error* methodology was successfully applied to NLH simulations accounting for 1, 2 or 3 harmonics and associated to different *Reynolds numbers*. The consideration of the interactions between the different flow quantities was adopted as a standard for all the multi-harmonic NLH computations presented in this section (Debrabandere, 2014). For all the cases, the $\Delta\alpha(\widetilde{F_y})$ identification criterion was based on the 1st considered harmonic. Fig. 5 shows the performance of the *phase error* method for all the analyzed configurations. As also observed by Spiker et al. (2006), a shifting towards higher St_{shnat} values was found when passing from 1 to 2 harmonics. The consideration of a third harmonic did not noticeably change the predicted St_{shnat}.

The identified St_{shnat} are compared with the experiments of Williamson (1996) and Fey et al. (1998) in Fig. 6. To contextualize this research, the results of a set of simulations performed by other authors were also included. All the computations did exhibit an underestimation of the predicted St_{shnat} with respect to the experimental references, probably due to the non consideration of three-dimensional flow effects. The St_{shnat} shifting observed in the application of the NLH *phase error* method in multi-harmonic simulations was found to improve this prediction. Nevertheless, even these

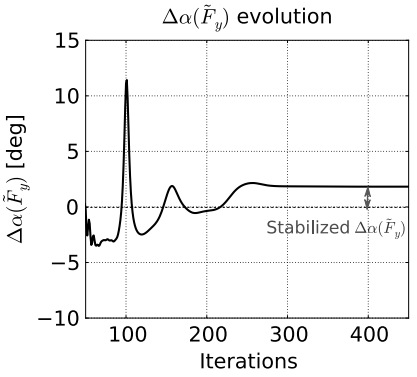

Fig. 4. Fixed cylinder, $\Delta\alpha(\widetilde{F_y})$ [deg] vs. NLH solver iterations. Simulation at $Re = 75$ and for a solved St of 0.139.

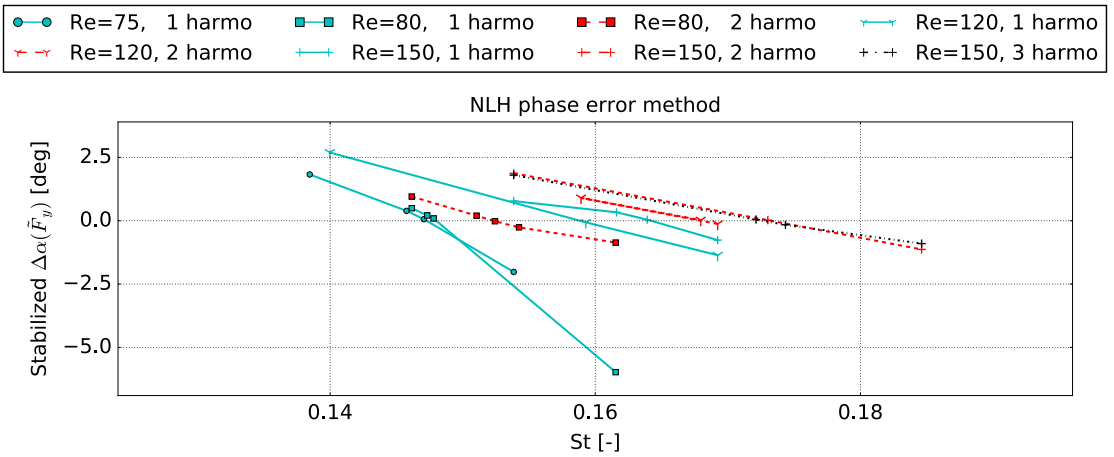

Fig. 5. Fixed cylinder, stabilized $\Delta\alpha(\widetilde{F_y})$ for different solved *Strouhal* and *Reynolds* numbers.

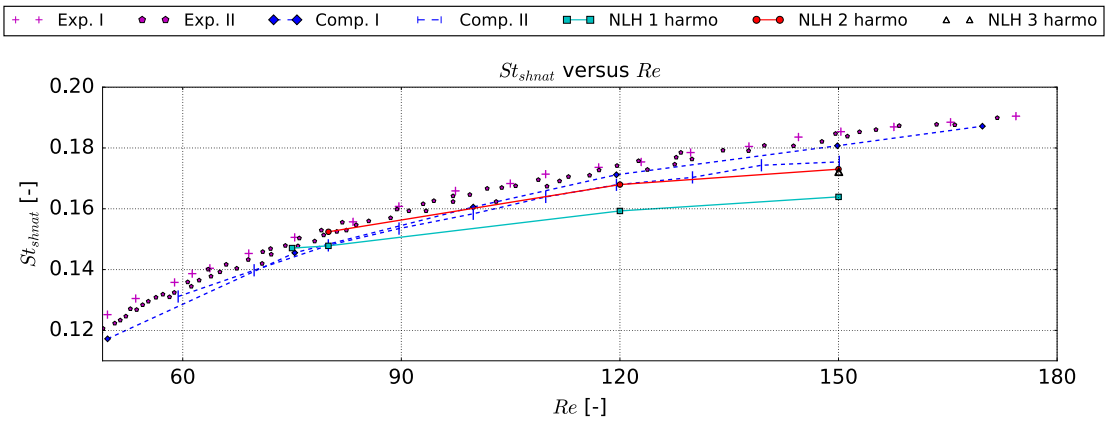

Fig. 6. Fixed cylinder, comparison of identified St_{shnat}. Exp. I refers to the experimental data from Williamson (1996). Exp. II refers to the experiments of Fey et al. (1998). Comp I. refers to the computational results of Spiker et al. (2006) using the *Harmonic balance* method. Comp. II refers to the computational results of McMullen (2003) using the *Non-Linear Frequency Domain* approach. NLH 1, NLH 2 and NLH 3 harmo refer to the present NLH simulations, accounting respectively for 1, 2 and 3 harmonics.

computations observed considerable underestimations for the highest *Reynolds numbers*, reaching up to approximately 7% for $Re = 150$. A feasible explanation for this issue could be the influence of the mesh resolution in the farfield, as pointed out in McMullen (2003). Another possible cause could be the impact of the size of the domain, as mentioned in Besem (2015) and Placzek et al. (2009).

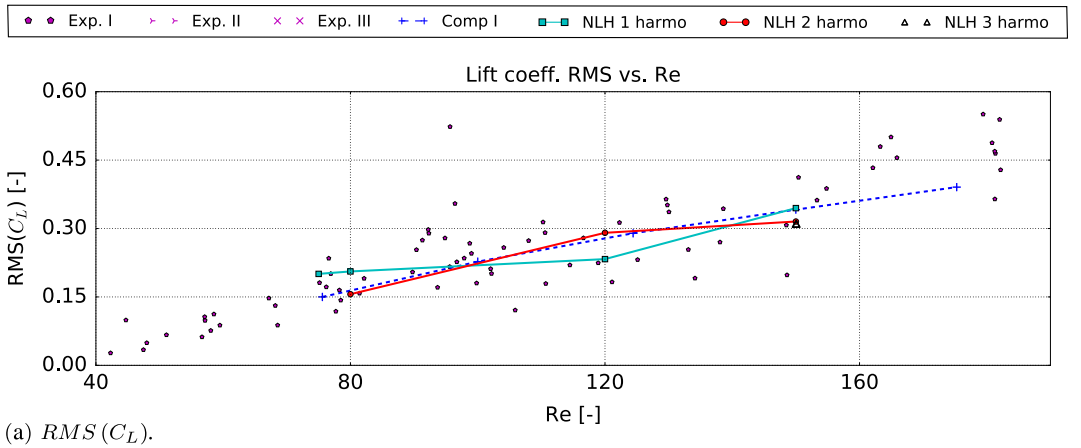

(a) $RMS\,(C_L)$.

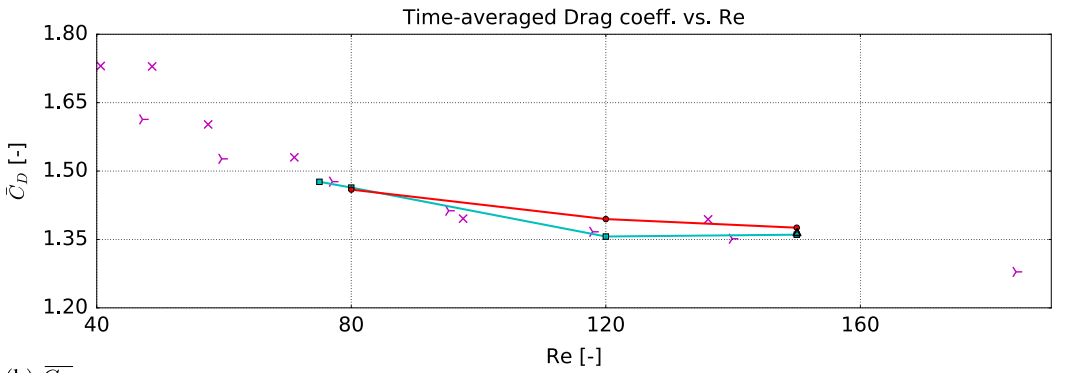

(b) $\overline{C_D}$.

Fig. 7. Fixed cylinder, comparison of computed load coefficients. Exp. I refers to the experiments collected by Norberg (2001). Exp. II refers to the experiments included in Wieselberger (1921). Exp. III refers to the experiments of Hoerner (1965). Comp. I refers to the numerical simulations of Spiker et al. (2006) with the *Harmonic Balance* method. NLH 1, NLH 2 and NLH 3 harmo refer to the present NLH simulations, accounting respectively for 1, 2 and 3 harmonics.

Obtained cylinder loads were also compared with experimental references. The *Root Mean Square* (RMS) values of the lift coefficient are shown in Fig. 7a. An important scatter is observed in the experimental data, related to the complexity of the shedding phenomenon. However, it can be concluded that the performed computations properly captured the evolution of *RMS* (C_L) with respect to the *Reynolds number*. Considerable discrepancies were observed for the single harmonic NLH computations with respect to the other simulations performed. This issue was certainly due to the non consideration of the second harmonic, that also led to an underestimation of St_{shnat}. A fair agreement was also found when comparing the NLH predictions with the results of the *Harmonic Balance* method computations of Spiker et al. (2006), with maximum observed differences of around 13%. Averaged drag coefficients are displayed in Fig. 7b, including the results of two experimental studies. A good agreement between experimental and computational data was found, even when considering single harmonic simulations. Bigger differences were observed at high *Reynolds numbers*, with an approximate maximum of 3% at $Re = 150$.

3.2. Results for the free oscillation configuration

In order to assess the performance of the proposed *2-way coupling* FSI methodology, the single degree of freedom aeroelastic system sketched in Fig. 8 was analyzed. This problem is referred to in the literature as the VIV of a cylinder in transversal oscillation (Griffin et al., 1973). All the computations were performed at $Re = 120$. The elastic system was introduced in FINE™/Turbo through an artificial structure mode, characterized by a natural frequency of oscillation f_k and a damping ratio ξ. The same mass m was considered for all the simulations. In order to allow the comparability with other experiments, it is interesting to express this variable in terms of the *reduced mass* m^*:

$$m^* = \frac{m}{\frac{1}{2}\rho D^2 L} = 7.49. \tag{17}$$

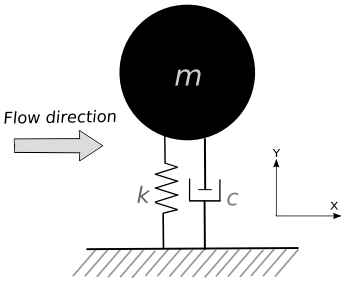

Fig. 8. Sketch of the elastic system attached to the cylinder in free oscillation.

Table 2
Free oscillation cylinder. Matrix of performed computations.

f_k/f_{shnat}	ξ			
1.00	0	0.0012	0.03	0.1
1.06			0.03	
1.22			0.03	

In this paper, the impact of two different aspects of the VIV phenomenon was analyzed:

- The spring stiffness: by means of the ratio f_k/f_{shnat}, where f_{shnat} refers to the natural shedding frequency computed for the fixed cylinder case in Section 3.1.
- The structural damping ratio of the elastic system ξ.

In order to target the zone corresponding to the amplification of the cylinder displacements, values of f_k/f_{shnat} slightly higher than the unity were tested. This choice relied on the observations of Placzek et al. (2009) and Anagnostopoulos and Bearman (1992). A base light damping of 3% was studied for all the cases. For the particular case of $f_k/f_{shnat} = 1.0$ three additional damping ratios were tested, including undamped and relatively high damped scenarios. Table 2 presents the studied test cases matrix.

The results issued from the present research were compared with the numerical studies of Shiels et al. (2001) and Placzek et al. (2009) at $Re = 100$. The milestone of both publications was the relation of the cylinder response to the so called *effective stiffness* k^*_{eff}, that combines the effects of the spring stiffness, the damping ratio and the cylinder mass. In particular, k^*_{eff} is defined as:

$$k^*_{eff} = k^* - 4\pi^2 f^{*2} m^* \tag{18}$$

where k^* is the dimensionless rigidity of the cylinder and f^* refers to the non-dimensioning of the observed shedding frequency f_{shed}:

$$k^* = \frac{k}{\frac{1}{2}\rho U_\infty^2 L}; \tag{19}$$

$$f^* = \frac{f_{shed} D}{U_\infty}. \tag{20}$$

Based on the results of Section 3.1 for the fixed cylinder configuration, only simulations accounting for 2 harmonics were performed. The mesh was deformed via the RBF+TFI method. As for the fixed cylinder case, the first solved harmonic frequency (corresponding to f_{shed}) was not known a priori. Contrary to the fixed configuration, the choice of an inappropriate f_{shed} was not manifested as an important value of $|\Delta\alpha(\widetilde{F_y})|$. However, an analogous phase shifting was observed for the harmonic cylinder displacement $\widetilde{D_y}$ for every evaluation of the aeroelastic equilibrium equations. The corresponding value of $\Delta\alpha(\widetilde{D_y})$ showed a stabilization after approximately 500 iterations. Inspired in the procedure followed for the identification of f_{shnat}, an iterative methodology was set-up in order to minimize the value of $|\Delta\alpha(\widetilde{D_y})|$. A maximum of 1° was chosen as a convergence criterion. This technique was applied to all the studied configurations in order to find the associated f_{shed} (see Fig. 9).

The simulations corresponding to the final identified f_{shed} verified the double criteria defined in this study ($|\Delta\alpha(\widetilde{F_y})| < 0.1°$ and $|\Delta\alpha(\widetilde{D_y})| < 1°$). Table 3 compiles the computed values of f_{shed} and k^*_{eff}, together with the cylinder loads coefficients C_L and C_D and the observed cylinder displacements D_y. The variables are expressed based on their time-average value and the corresponding fluctuating part, denoted by the superscripts $^-$ and $'$, respectively. It is important to remark that the value of k^*_{eff} was understood as an output of the simulation, due to its dependence to the shedding frequency f_{shed}.

Fig. 10a shows the computed maximum cylinder displacements, expressed as a function of k^*_{eff} and compared with the results of other authors. An amplification of the displacement amplitudes can be observed in the range $k^*_{eff} = [0; 5]$

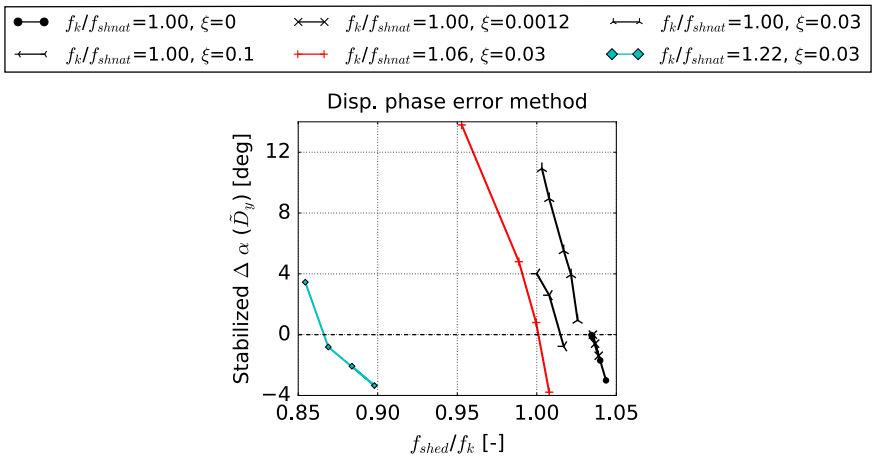

Fig. 9. Free oscillation cylinder, stabilized $\Delta\alpha(\widetilde{D}_y)$ for different NLH (2 harmonics) computations as a function of f_{shed}/f_k. A dashed line corresponding to $\Delta\alpha(\widetilde{D}_y) = 0$ was included.

Table 3
Summary of free oscillating cylinder variables. All quantities are non-dimensional.

Input variables		Output variables					
f_k/f_{shnat}	ξ	$(f_{shed}D)/U_\infty$	$\bar{C}_D$	$C'_{D,\max}$	$C'_{L,\max}$	$D'_{y,\max}/D$	k^*_{eff}
1.00	0	0.174	1.59	0.041	0.148	0.256	−0.59
	0.0012	0.174	1.59	0.041	0.147	0.255	−0.58
	0.03	0.172	1.57	0.029	0.167	0.233	−0.43
	0.1	0.171	1.54	0.036	0.305	0.169	−0.29
1.06	0.03	0.178	1.63	0.074	0.145	0.258	0.01
1.22	0.03	0.185	1.54	0.088	0.906	0.296	3.27

for the simulations of Shiels et al. (2001) and Placzek et al. (2009). This region is known in the literature as the *lock-in region*. By analyzing the results issued from the present work, two main groups can be distinguished. On the one hand, the computations accounting for $f_k/f_{shnat} = 1.00$ and $f_k/f_{shnat} = 1.06$ showed values of the effective stiffness in the vicinity of 0.0, corresponding to the beginning of the displacements amplification. On the other hand the $f_k/f_{shnat} = 1.22$ simulation was associated to a k^*_{eff} value of 3.27, where the cylinder amplitudes start to decrease. For the sake of simplicity in this paper, these zones are referred to as the *pre lock-in region* and the *post lock-in region* respectively. The results obtained with the NLH-based *2-way coupling* FSI approach followed the trend established by the time marching simulations of Shiels et al. (2001) and Placzek et al. (2009). The comparison of both methodologies points out towards a possible error in the computation of k^*_{eff} for the harmonic simulations. This fact could be attributed to the uncertainty in the prediction of f_{shed}. As it was observed in Section 3.1 regarding the computation of the fixed configuration shedding frequency f_{shnat}, numerical aspects such as the size of the domain or the mesh resolution could influence this estimation. Another feasible explanation to the k^*_{eff} shifting could be the difference in the considered *Reynolds number*, which is not taken into account by the effective stiffness parameter and can have an impact on the width of the *lock-in region*. This issue should be confirmed by performing additional simulations aiming to capture the maximum of the cylinder oscillations amplitude. Fig. 10b shows the corresponding values for $C'_{L,max}$. The increase of the lift fluctuations in the *lock-in region* region predicted by Shiels et al. (2001) and Placzek et al. (2009) was reproduced by the proposed NLH-based methodology. The point laying in the *post lock-in region* was found to be shifted to a lower k^*_{eff} value with respect to the results of both publications. Fig. 10c depicts a comparison of the average drag coefficient. As for the lift harmonic, a monotonic increase of $\bar{C}_D$ was obtained by Shiels et al. (2001) and Placzek et al. (2009) in the *pre lock-in region*. This behavior was reproduced in the computations performed in the present work. Contrary to the lift fluctuation, a fair agreement with respect to the numerical references was also found for the computation located after the drag crisis. Finally, the values of f_{shed} normalized by f_{shnat} are illustrated in Fig. 10d, where a good agreement between all the simulations can be also observed.

4. Industrial application: study of the DTU 10 MW RWT dynamic aeroelasticity

Due to the confidentiality of wind turbine manufacturers with regards to their designs, the research community should often rely on the so-called *academic* or *reference* HAWTs for the validation of the developed numerical models. The first complete and publicly available HAWT was the NREL Phase VI, that accounted for a 10 m diameter rotor. The experimental database generated for this design was used for the validation of almost every CFD code applied to the simulation of HAWTs,

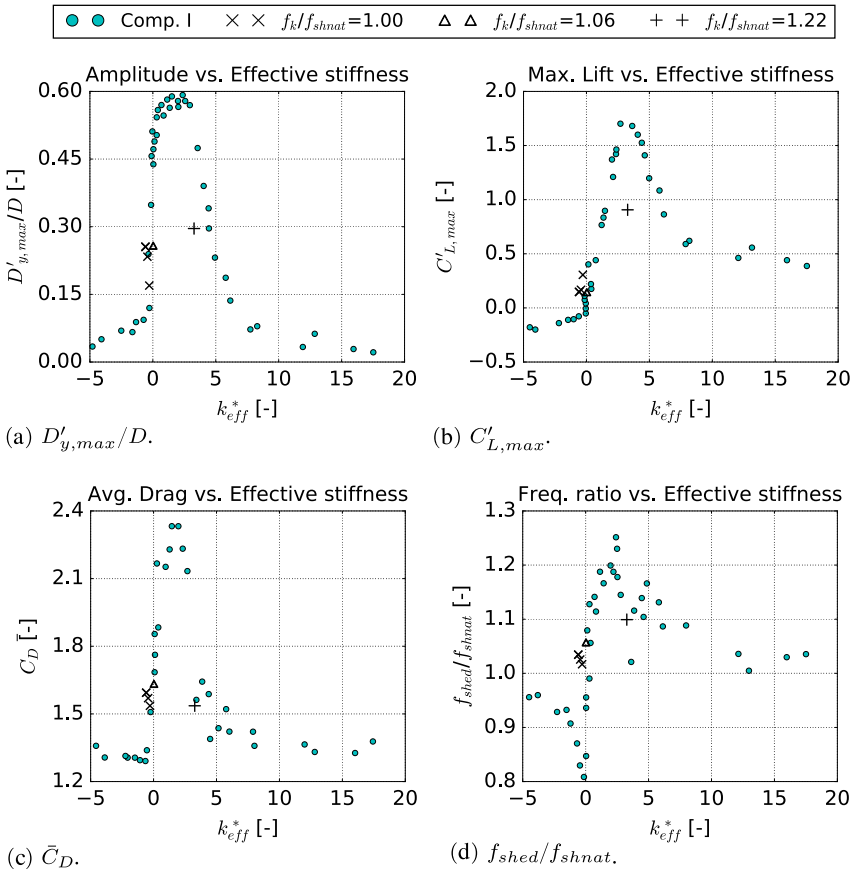

(a) $D'_{y,max}/D$. (b) $C'_{L,max}$. (c) $\bar{C}_D$. (d) f_{shed}/f_{shnat}.

Fig. 10. Computed variables for the free oscillating cylinder as a function of k^*_{eff}. NLH computations performed at $Re = 120$ and accounting for 2 harmonics. Comp. I combines the results of the simulations of Shiels et al. (2001) and Placzek et al. (2009) at $Re = 100$.

as summarized by Hansen et al. (2006). Complementary *reference* HAWTs followed the same path established by the NREL Phase VI, such as the MEXICO model, a design accounting for a 4.5 m rotor diameter (Schepers and Snel, 2007). The wind tunnel experiments performed for this model extended the CFD code validation possibilities, especially when focusing in wake analysis. The NREL 5 MW *reference* wind turbine, with a rotor diameter of 126 m, was developed in order to achieve a deeper understanding of the offshore environment (Jonkman et al., 2009). Even under the limitation of the absence of experimental data, it has been widely used for research purposes. In particular, the NREL 5 MW has served as a basis for a series of aeroelastic packages code-to-code comparison projects focused in the study of bottom-fixed and floating offshore configurations (Jonkman and Musial, 2010; Jonkman et al., 2012; Robertson et al., 2013, 2015). The NREL 5 MW was recently upscaled in order to design a publicly available 10 MW reference wind turbine referred to as DTU 10 MW RWT (Bak et al., 2013). With a rotor of 178.3 m, the aim of this 3-bladed model is to provide the research community with a large rotor design, representative of the new generation of MW wind turbines. One of the challenges expected for this HAWT size is the predominant role of the rotor aeroelasticity effects, due to the slenderness and flexibility of the blades. This justifies the choice of the DTU 10 MW RWT for the application of the *2-way coupling* FSI methodology developed in the present work. As for the NREL 5 MW, no full scale experimental data is available for this wind turbine model. Hence, the results included in the present work aim to constitute a basis for future benchmarks concerning the dynamic aeroelasticity of this HAWT.

The DTU 10 MW RWT equips the FFA-W3 airfoil series along the whole span. The tower is made from steel, and it has a height of 115.63. Two variants of the DTU 10 MW RWT blade geometry were defined in Bak et al. (2013), considering a *straight* and a *pre-bent* axis. In Horcas et al. (2016a) the solutions of two 3D RANS computations of the isolated rotor were compared, assuming a *straight* blade configuration. One simulation employed the FINE™/Turbo solver and was performed by the authors of this paper, while the other was carried out by Bak et al. (2013) with Ellipsys3D. Fig. 11 shows the computed DTU 10 MW RWT rotor loads for both solvers. The different solutions captured a similar monotonic increase of both thrust and power for the considered operating range. The maximum relative difference between the results of both solvers was found to be below 1.5%. A more realistic geometry was studied by the authors of the present work in Horcas et al. (2016b). Both the rotor pre-bending and the tower geometry were considered in the DTU 10 MW RWT assembly. The introduction of the tower in the mesh forced the flow solution to be inherently unsteady, and the authors proposed the use of the NLH method

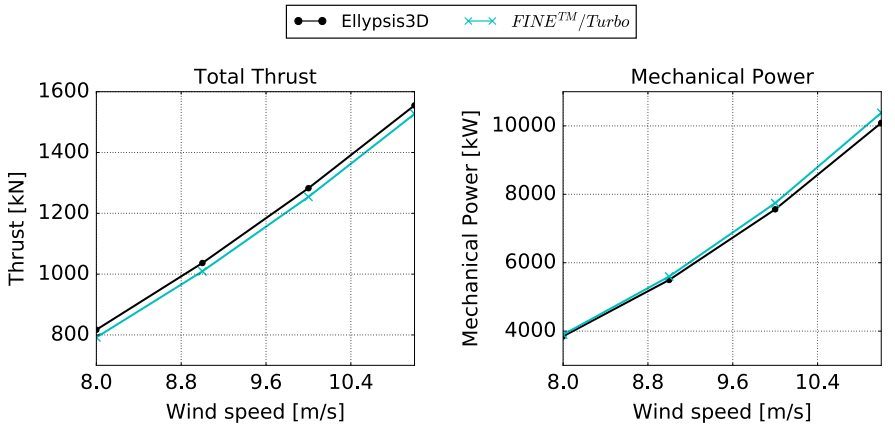

(a) Rotor thrust. (b) Rotor power.

Fig. 11. DTU 10 MW RWT total loads versus wind speed, original isolated rotor configuration accounting for *straight* blades. Ellipsys3D refers to the CFD computations included in Bak et al. (2013). FINE™/Turbo refers to the results included in Horcas et al. (2016a) and performed with the present solver.

for the first time in a HAWT context. As a first approach, the blades were assumed to be *rigid*. In the present publication the numerical model is enhanced by the consideration of blade flexibility, in order to study the dynamic aeroelasticity of the DTU 10 MW RWT. To put in evidence the influence of the aeroelastic effects the results issue from this simulation are compared with two additional computations, both assuming a *rigid* rotor. While one considered the full machine, the other modeled the isolated rotor. An optimal operating point was simulated, characterized by an incoming wind speed of 10.5 m.s^{-1}, a rotor speed of 8.836 RPM and a 0° pitch angle. For this configuration, a maximum relative *Reynolds number* of 1.28×10^7 is to be expected. Spalart–Allmaras turbulence model was used for all the presented simulations (Spalart and Allmaras, 1992).

4.1. Considered geometry

Fig. 12 illustrates the main geometrical properties of the studied DTU 10 MW RWT assembly, as defined in Bak et al. (2013). A tilt angle of 5°was considered between rotor and tower axes. Blades accounted for a pre-cone angle of 2.5°, as well as a distributed pre-bending. Based on the disadvantageous effects on rotor performance found in the work of Horcas et al. (2016a), the *Gurney flaps* were removed from the original blade geometry.

In order to present the unsteady results of this paper, the azimuth angle θ and the normalized time t/T were used. In this context, t is defined as the already elapsed time in the current revolution and T refers to the period of rotation. The DTU 10 MW RWT operates in clockwise rotation, and it is assumed that at $t/T = \theta = 0$ one of the blades is aligned in its down position with the tower axis. This particular blade, displayed in dark gray in Fig. 12, is referred to in this document as the *observed blade*.

4.2. Considered meshes

The structured grid generator Autogrid5™ (NUMECA International, 2016a) was used in order to create two different meshes:

- **1B**: Devoted to the analysis of the isolated rotor, this mesh accounted for a single blade passage of the DTU 10 MW RWT, including the original nacelle and the hub geometries. The definition of this grid was extracted from Horcas et al. (2016a), where the results of the used solver were in good agreement with another 3D RANS solution (see Fig. 11). A first cell height of 10^{-4} m was imposed on the blade, in order to target a minimum of 30 points in the boundary layer and y+ values of less than 10 at the first inner cell (NUMECA International, 2016b). The resulting mesh had a total of 7 million nodes.
- **1B-1T**: This mesh can be seen as an extension of the 1*B* grid in order to perform simulations of the complete DTU 10 MW RWT machine with the NLH method, as previously shown in Horcas et al. (2016b). A radial *rotor/stator interface* crossing the nacelle was defined in order to allow the introduction of the tower mesh. The same blade grid topology of 1*B* was used, and a single blade passage was meshed for the rotor. A 360° grid was generated for the tower side, also accounting for a first cell height of 10^{-4} m. The resulting mesh had a total of 13 million nodes.

The same computational domain size was considered for both meshes (see Fig. 13). Flow inlet and outlet were respectively located at 2.2*R* and 3.1*R* from the origin of coordinates. Non-periodic boundary conditions, referred to as *externals*, relied in the subsonic far-field formulation described in Hirsch (1990). As a first approach and in order to keep the rotational periodicity of the problem, the incoming wind was assumed to be aligned with the rotor axis. A contraction angle was

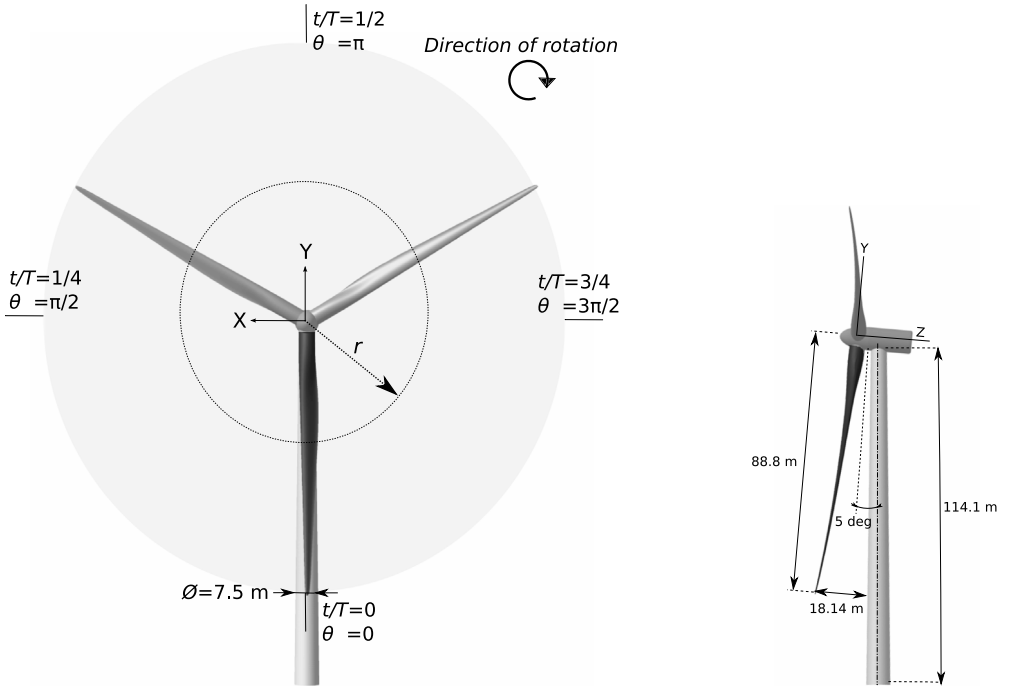

(a) Front rotor view. (b) Side view.

Fig. 12. Sketch of the DTU 10 MW RWT assembly. The *observed blade* was displayed in dark gray.

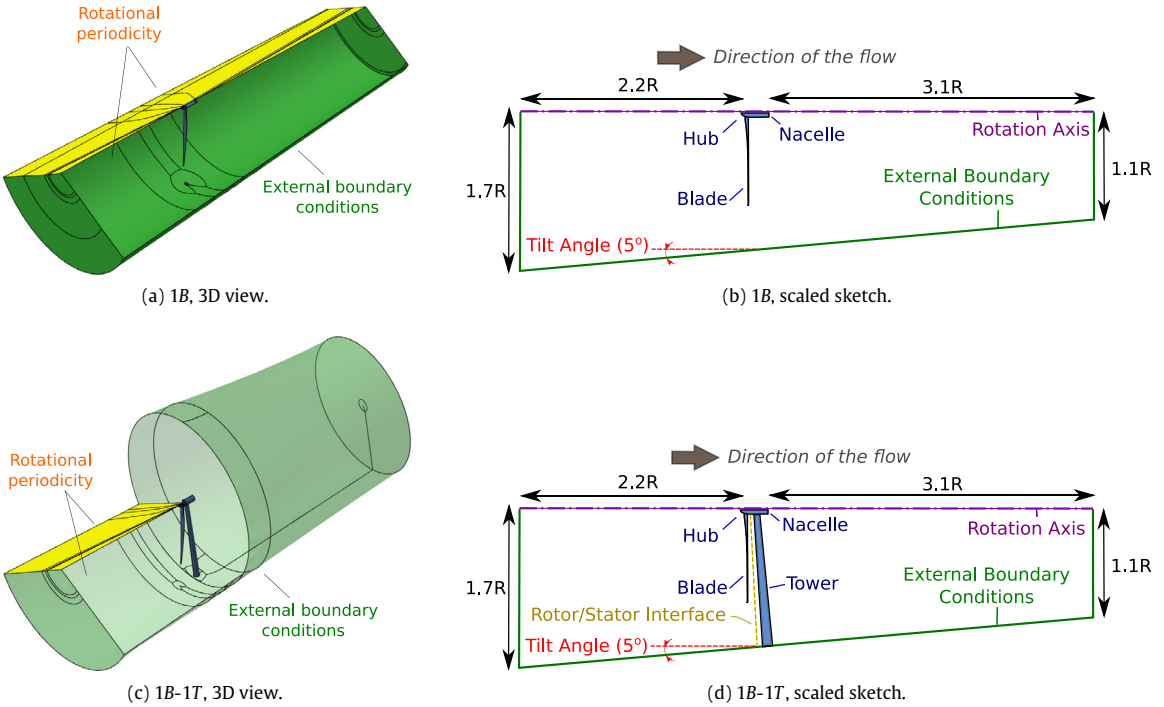

(a) 1*B*, 3D view. (b) 1*B*, scaled sketch.

(c) 1*B*-1*T*, 3D view. (d) 1*B*-1*T*, scaled sketch.

Fig. 13. Description of the computational domains for 1*B* and 1*B*-1*T* meshes. Solid lines represent mesh blocking. In (a) and (c), one of the periodic boundary conditions was removed to allow the visualization of the interior of the domain. In (c), the domain of the tower side was set to translucent to get a clearer visualization.

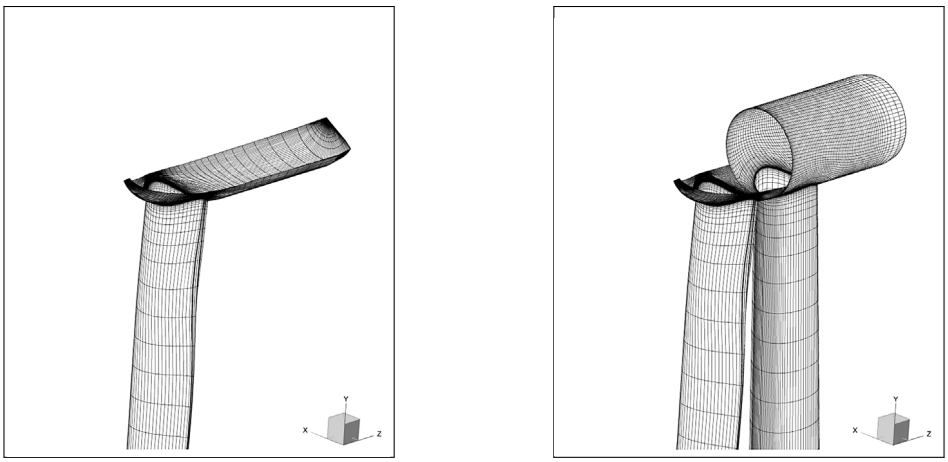

(a) 1*B* mesh. (b) 1*B*-1*T* mesh.

Fig. 14. Detail of the DTU 10 MW RWT surface meshes. 1 out of 2 grid lines were skipped.

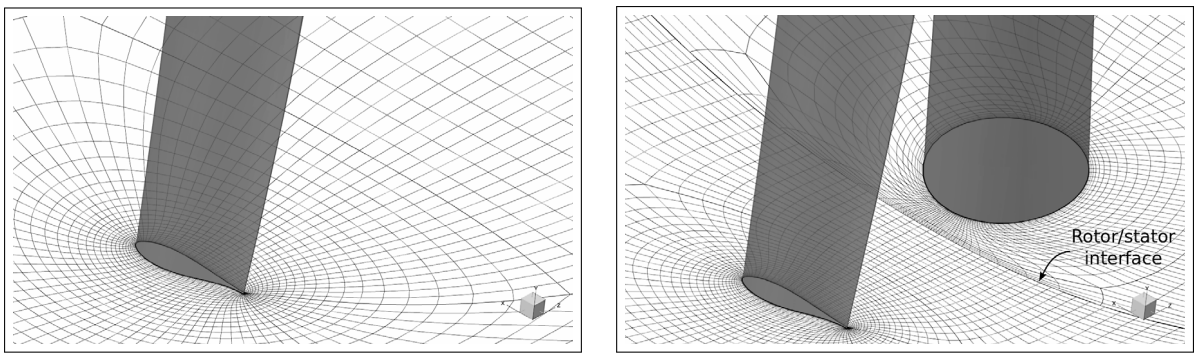

(a) 1*B* mesh. (b) 1*B*-1*T* mesh.

Fig. 15. DTU 10 MW RWT cross-section meshes closest to $r/R = 0.5$. 1 out of 2 grid lines were skipped.

imposed in the longitudinal direction of the domain. This angle was assumed to be the *tilt* angle, in order to achieve an orthogonal intersection with the tower axis for the 1*B*-1*T* mesh.

Fig. 14 illustrates the surface meshes for every configuration. Fig. 15 displays the cross-section meshes corresponding to the grid line closest to $r/R = 0.5$ (i.e. half of blade span). For clarity purposes, only 1 out of 2 grid lines are shown in both figures.

1*B* and 1*B*-1*T* meshes were used in order to perform three different simulations, labeled in this publication as *Rotor only rigid*, *Full machine rigid* and *Full machine flexible*. A short description of these computations is included in the next section, followed by a discussion of their results.

4.3. Computational settings

This section presents the computational settings of the performed DTU 10 MW RWT simulations. Details of the fluid model are given. If applicable, the considered structural model of the wind turbine rotor is also described.

4.3.1. Rotor only rigid simulation

This computation was devoted to the study of the steady aerodynamics of the isolated rotor. The RANS method was applied on the 1*B* mesh. The hypothesis of *rigid* blades was made.

4.3.2. Full machine rigid simulation

This computation aimed to analyze the influence of the presence of the tower on the rotor performance. As for the *Rotor only rigid* simulation, the blades were assumed to be *rigid*. A NLH method simulation based of the 1*B*-1*T* mesh was performed.

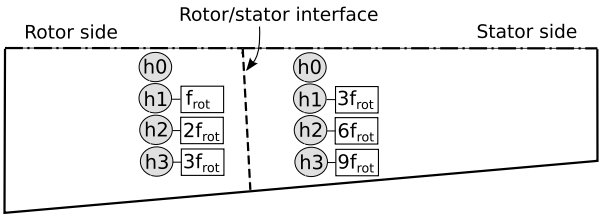

Fig. 16. Diagram of the harmonics involved in *Full machine rigid* and *Full machine flexible* computations. Gray circles contain the harmonic index *hx*, where *h*0 stands for the time mean. Square boxes indicate the frequency attached to every harmonic, with respect to the rotor frequency f_{rot}.

Table 4
Summary of the DTU 10 MW RWT blade structure model used in the *Full machine flexible* simulation.

Mode Id., *k*	1	2	3	4	4	6
Mode description	1st flap	1st edge	2nd flap	2nd edge	3rd flap	1st torsion
Mode Frequency [Hz]	0.641	0.965	1.780	2.879	3.606	5.678
Damping ratio	0.03	0.03	0.084	0.089	0.17	0.208

A full non-matching non-reflecting approach was used for the modeling of the *rotor/stator interface* (Vilmin et al., 2006). As for a classical turbomachinery application of the NLH method, the frequency of the fundamental harmonic for the rotor and stator sides was determined by the BPF of the adjacent bladerow. By using the relations outlined in Table 1 and assuming a null rotational speed for the stator side, these fundamental harmonic frequencies corresponded to f_{rot} and $3f_{rot}$ respectively (being f_{rot} the frequency of the rotor). For the considered operating point, where the imposed rotor speed was 8.836 RPM, the value of f_{rot} corresponded to 0.147 Hz. A study of the influence of the total number of harmonics for this DTU 10 MW RWT configuration was already presented in Horcas et al. (2016b), including a comparison with the results of the time-marching approach URANS. In that publication the authors identified the potential effects of the tower as the main source of flow unsteadiness. A total of 3 harmonics was found enough to properly estimate the influence of this unsteadiness on the rotor loads. A low span *blade shedding* was also identified, which frequency corresponded to the 5th harmonic. In order to reduce the required computational time, this local effect was neglected in the present work. It was then decided to consider a total of 3 harmonics for the *Rotor only rigid* simulation. Fig. 16 summarizes the solved harmonic frequencies for both sides of the *rotor/stator interface*.

4.3.3. Full machine flexible simulation

The objective of this computation was to assess the impact of the dynamic aeroelasticity on the rotor performance. As for the *Full machine rigid* simulation, the 1*B*-1*T* mesh of the complete DTU 10 MW RWT assembly was used. The computation procedure relied on the *2-way coupling* FSI methodology presented in Section 2.2. A reduced order model of the DTU 10 MW RWT structure, defined by a set of natural frequencies and mode shapes, was coupled to the flow loading computed by the NLH solver. The mesh was deformed with the IDW method.

Prior to the FSI simulation, a modal basis of the DTU 10 MW RWT blade structure was computed with the commercial package Abaqus (Simulia, 2008). A publicly available model based on the *Finite Element Method* (FEM) was used for this task (Bak et al., 2013), accounting for the blade pre-bending as suggested in Horcas et al. (2016a). The DTU 10 MW RWT blade is made from glass fiber reinforced composites and balsa wood, used as a sandwich core material. In the FEM model of Bak et al. (2013), the composite layup of the blade was defined as a stacking-sequence of layers, acting as multidirectional plies (i.e. each ply containing fibers with multiple orientation angles). The structural design accounted for a load carrying box girder with two shear webs. A third shear web was included at the vicinity of the trailing edge, from a radius of 21.8 m up to the blade tip. External and internal geometries of the blade and composite layup were modeled by means of 8-node layered shell elements. The adhesive connecting the suction side shell and the pressure side shell was modeled by means of hexahedral elements. The whole FEM model accounted for a total of 35,000 elements and 104,000 nodes. In order to properly define the composite layup, the blade was split into 11 circumferential regions and 100 radial regions. A 3D view of the whole FEM model is depicted in Fig. 17. In the extraction of the structure modal basis, the centrifugal stiffening effects associated to the studied rotor RPM were taken into account. To reduce the computational time of the *2-way coupling* FSI simulation, only the first 6 modes were used (i.e. the 1st, 2nd and 3rd flapwise, the 1st and 2nd edgewise and a torsion mode). A damping coefficient was considered for each of the selected modes, based on the estimated values included in Bak et al. (2013). Table 4 summarizes the main characteristics of the DTU 10 MW RWT blade structure model.

As for the *Full machine rigid* simulation, only the first three harmonics associated to the BPF were considered in the NLH solver for this aeroelastic computation (Fig. 16). As a consequence, the frequencies of the blade response corresponded to multiples of the rotor frequency. This assumption relied on the hypothesis that, for the considered operating point, the most important blade deflections are to be synchronized with the *blade–tower alignment* event. The contribution of the structural frequencies to the blade response was then neglected in the present simulation.

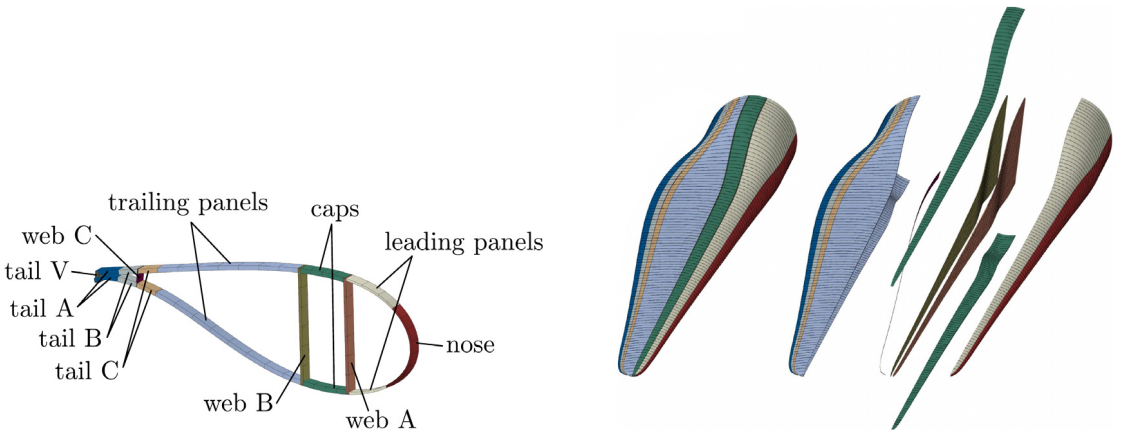

(a) Radial segment. (b) Whole assembly.

Fig. 17. DTU 10 MW RWT blade FEM model. (a) Detail of every radial segment, accounting for 11 circumferential regions. (b) Global view of the assembly, including the 100 radial segments.
Source: Reproduced from Bak et al. (2013).

Table 5
Computed global rotor loads for *Rotor only rigid* computations based on 1*B* and *1B coarse* mesh variants.

Mesh	1*B coarse*	1*B*	Diff. [%][a]
Thrust [kN]	1,478.8	1,440.4	−2.6
Power [kW]	9,664.5	9,570.0	−1.0

[a] Diff. refers to the relative load variation when passing from *1B coarse* to 1*B* meshes.

Table 6
Computed generalized displacements of the DTU 10 MW RWT blade, *Full machine flexible* simulation.

		Mode Id.					
		$k=1$	$k=2$	$k=3$	$k=4$	$k=5$	$k=6$
Time-averaged	$\bar{q}_k$	−283.48	12.665	6.0119	0.7770	1.6042	0.3672
First harmonic	$\mathrm{Re}(\tilde{q}_k\|_1)$	1.1230	0.0564	0.0304	−0.0058	−0.0047	−0.0052
	$\mathrm{Im}(\tilde{q}_k\|_1)$	−0.5236	0.0327	0.0204	−0.0032	−0.0015	−0.0012
Second harmonic	$\mathrm{Re}(\tilde{q}_k\|_2)$	0.8524	0.0477	0.0500	−0.0068	−0.0051	−0.0042
	$\mathrm{Im}(\tilde{q}_k\|_2)$	−0.8561	0.0296	0.0206	−0.0024	0.0009	−0.0001
Third harmonic	$\mathrm{Re}(\tilde{q}_k\|_3)$	0.3889	0.0468	0.0768	−0.0090	−0.0062	−0.0035
	$\mathrm{Im}(\tilde{q}_k\|_3)$	−1.0558	0.0349	0.0037	−0.0020	−0.0005	−0.0008

4.4. Influence of the mesh

The *Rotor only rigid* simulation was used in order to analyze the sensitivity of the considered grids. For this purpose, a *coarse* version of the 1*B* mesh was generated. This grid, referred to as *1B coarse*, was created by merging each 8 volume cells of the 1*B* mesh into 1 (2 in each direction). The total number of mesh nodes for *1B coarse* was 9×10^5, corresponding to approximately 1/8th of the grid points of 1*B*. Table 5 reproduces the global rotor loads for two *Rotor only rigid* computations based on both mesh variants. The observed global rotor loads difference was below 3% for the studied operational point, concluding that the base mesh 1*B* provides accurate enough results for the type of analysis to perform.

4.5. Results of full machine flexible simulation concerning blade deformation

Table 6 compiles the generalized displacements computed for the *Full machine flexible* simulation. As expected for the studied operating point, the main contribution was carried out by the first mode (i.e. the 1st flapping). This remark was valid for both the time-averaged and the harmonic contributions.

The resulting time-averaged deformed blade is depicted in Fig. 18, superposed to the original (i.e. undeflected) rotor geometry. As illustrated in Fig. 18b, a deformation parallel to the rotor axis d_p of 9.15%R was found at the blade tip (equivalent to 8.16 m). This deflection represents a margin of 54.3% with regards to the design tower clearance, and it is in line with the results of the static aeroelasticity study of the DTU 10 MW RWT isolated rotor presented in Horcas et al. (2016a). As a

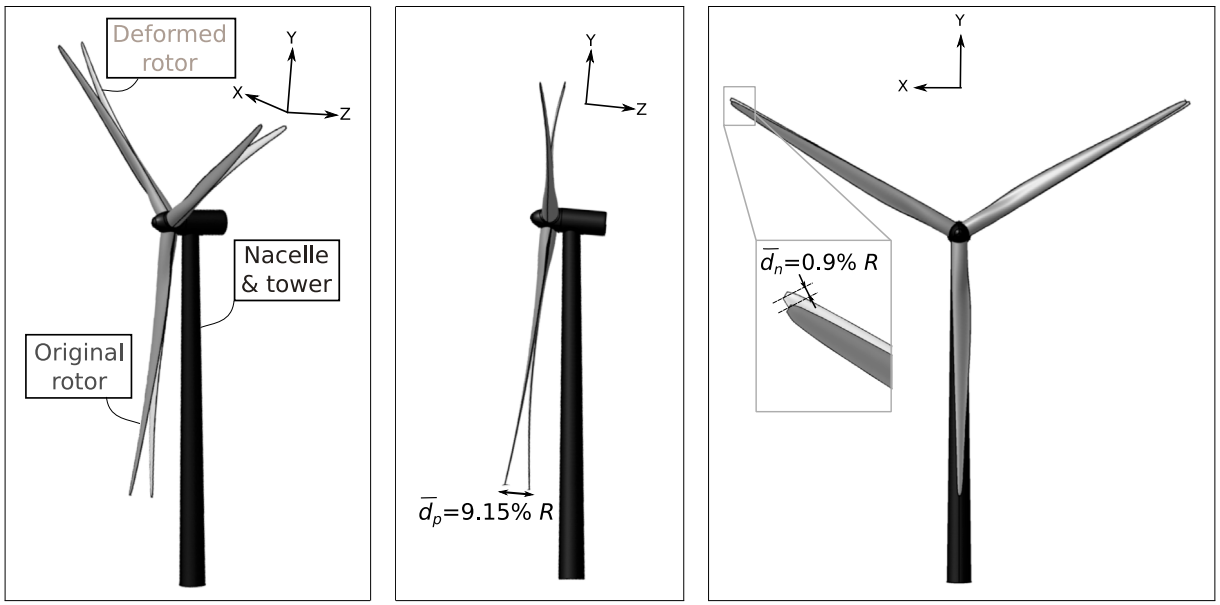

(a) 3D view. (b) Side view. (c) Front rotor view.

Fig. 18. 3D visualization of the time-averaged deformed rotor for the *Full machine flexible* simulation of the DTU 10 MW RWT, superposed to the original geometry. $\bar{d}_p$ stands for the time-averaged deformation parallel to the rotor axis (often referred to as out-of-plane or flap deformation in rotorcraft terminology). $\bar{d}_n$ stands for the time-averaged deformation normal to the rotor axis (often referred to as in-plane or lag deformation in rotorcraft terminology).

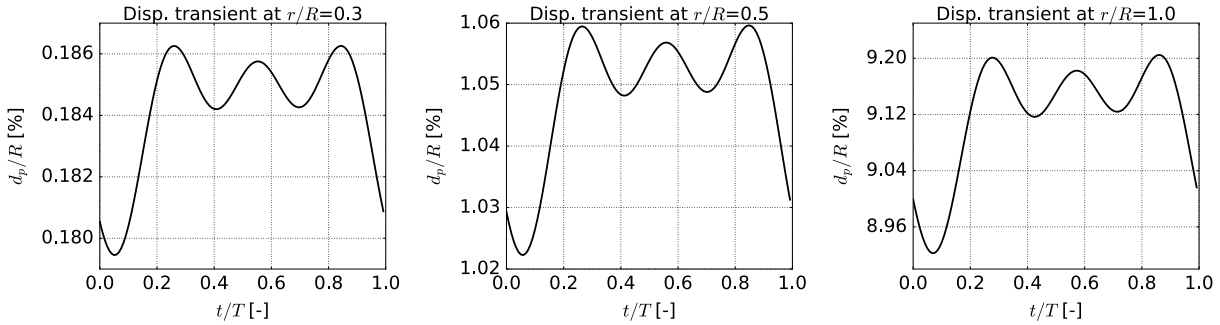

(a) $r/R = 0.3$. (b) $r/R = 0.5$. (c) $r/R = 1.0$.

Fig. 19. DTU 10 MW RWT *Full machine flexible* simulation, time evolution of d_p for points located at different radial positions of the *observed blade* leading edge.

consequence of the 1st flapping mode predominance, the deformation normal to the rotor axis $\overline{d_n}$ was found to be one order of magnitude lower than $\overline{d_p}$ (Fig. 18c).

Fig. 19 shows the time evolution of d_p for points located at different radial positions of the *observed blade* leading edge, normalized by the rotor radius *R*. The same fluctuation pattern was observed regardless the considered blade span, with a maximum deflection located slightly after the *blade–tower alignment* followed by a deformations stabilization. The magnitude of the peak-to-peak values of d_p was found to be relatively small with respect to the corresponding time-averaged deflections, with ratios laying on the range [3; 3.7]% all along the span. At the DTU 10 MW RWT blade tip, a time-averaged d_p of 9.15%*R* was observed. This is slightly higher than the corresponding value of 2.5%*R* computed for the NREL 5 MW in Hsu and Bazilevs (2012), as expected due to the different rotor size. When comparing the amplitude of oscillations of d_p at the blade tip, the *Full machine flexible* simulation predicted a value of 0.14%*R*, while 0.4%*R* was found by Hsu and Bazilevs (2012). This difference could be explained by the effects of the blade pre-bending, that was not considered in the latter simulation, or by the discrepancies in structural design parameters such as the damping.

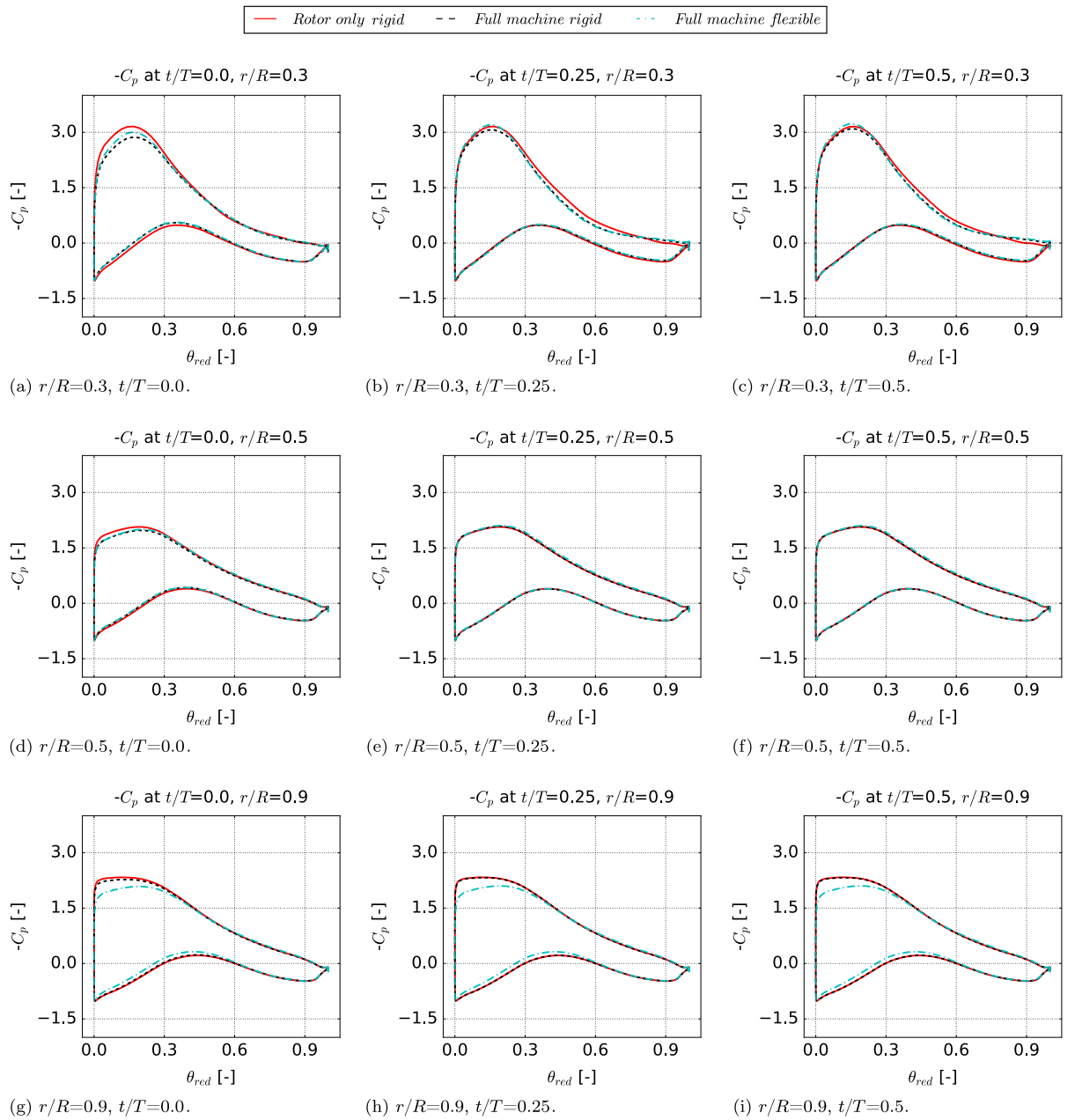

(a) r/R=0.3, t/T=0.0. (b) r/R=0.3, t/T=0.25. (c) r/R=0.3, t/T=0.5.

(d) r/R=0.5, t/T=0.0. (e) r/R=0.5, t/T=0.25. (f) r/R=0.5, t/T=0.5.

(g) r/R=0.9, t/T=0.0. (h) r/R=0.9, t/T=0.25. (i) r/R=0.9, t/T=0.5.

Fig. 20. Comparison of the computed pressure coefficient C_p around the DTU 10 MW RWT *observed blade* for different cross-sections and instants. The sign of C_p was inverted for all the graphs.

4.6. Results cross-comparison concerning blade and rotor loading

Fig. 20 shows a comparison of the pressure coefficient C_p computed around the *observed blade* for several radial positions r/R and instants t/T. The results are expressed as a function of the reduced azimuthal angle θ_{red}, defined as:

$$\theta_{red} = \frac{\theta - \theta^{lead}}{\theta^{trail} - \theta^{lead}} \tag{21}$$

with θ^{lead} and θ^{trail} being the azimuthal angles of the leading and trailing edges, respectively.

When being compared with the results of *Rotor only rigid*, both *Full machine rigid* and *Full machine flexible* simulations exhibited a decrease of the performance of the suction side in the vicinity of $t/T = 0$. This fact can be attributed to the potential effects related to the presence of the tower, observed all along the blade. The temporal extension of this tower

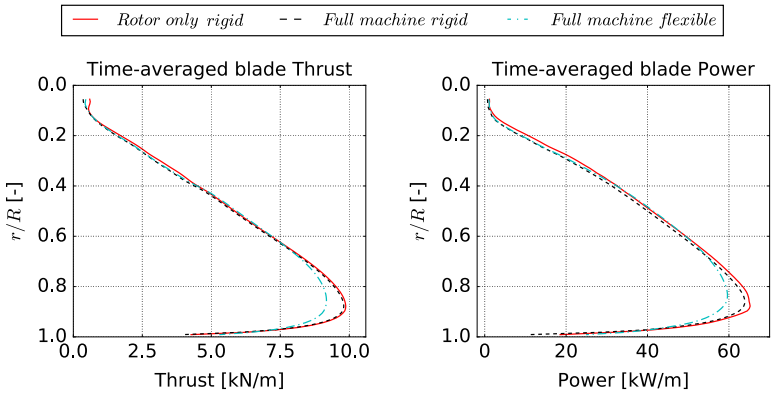

(a) Time-averaged blade thrust. (b) Time-averaged blade power.

Fig. 21. Comparison of the radial evolution of the time-averaged blade loads for the performed DTU 10 MW RWT simulations.

influence was found to be wider for the low span range, due to the more important ratio between the blade chord and the tower diameter. This is illustrated in the Fig. 20b and Fig. 20c, where significant differences with respect to the isolated rotor results are identifiable. The impact of the aeroelastic effects of the *Full machine flexible* simulation was especially important for the high span range. As it can be observed in the results of $r/R = 0.9$, a reduction of the performance of both pressure and suction sides was found regardless the considered instant t/T. This issue is related to the important time-averaged blade deflections already shown in Fig. 18.

Fig. 21 compares the radial evolution of the time-averaged blade loads. As expected from the analysis of the C_p distribution, due to the influence of the tower both *Full machine rigid* and *Full machine flexible* simulations observed a decrease of the computed loads for the whole blade span. This was especially true for the case of the time-averaged blade power. The impact of the blade flexibility was found to be more important than the influence of the tower, since a considerable loads reduction was predicted for *Full machine flexible* at high span range.

Fig. 22a and Fig. 22b show the time reconstruction of the *observed blade* loads for *Full machine rigid* and *Full machine flexible* simulations. The corresponding values of the *Rotor only rigid* computation were also included in the plots. As a consequence of the presence of the tower, a decay of both blade loads was observed in the vicinity of $t/T = 0$ for the two simulations based on the complete machine. It is interesting to assess the combined impact of the three blades on the global rotor loads (see Fig. 22c and Fig. 22d). Only the harmonics the order of which is a multiple of the number of blades did contribute to the rotor loads oscillation (see for instance Bielawa, 1992). Hence, a monochromatic signal was obtained for both *Full machine rigid* and *Full machine flexible*, which frequency corresponded to the third harmonic. Table 7 compiles the time-averaged values of the global rotor loads, together with the corresponding amplitudes of oscillation. For future reference, the results are expressed both in terms of absolute loads and non-dimensional coefficients. When compared to *Rotor only rigid*, the *Full machine rigid* computation observed decreases of 1.77% for the time-averaged rotor thrust and 3.62% for the time-averaged power. The additional rotor loads reduction of *Full machine flexible* associated to the consideration of the rotor aeroelasticity led to total decreases of 2.96% for the time-averaged thrust and 4.08% for the time-averaged power. The modeling of the blade flexibility also had an attenuating effect on the loads fluctuation. While for *Full machine rigid* the amplitude of oscillations of the rotor thrust represented 0.92% of its time-averaged value, the corresponding ratio for *Full machine flexible* simulation was only 0.66%. For the case of the rotor power, analogous ratios of 1.95% for *Full machine rigid* and 1.12% for *Full machine flexible* were predicted.

4.7. Comments about the computational time

Table 8 lists the computational resources that were used for the simulations performed in this work. A prediction of the required time for a computation of the unsteady aerodynamics of the complete DTU 10 MW RWT by means of the standard URANS method was included under the label *Full machine rigid-URANS*. This estimation relied on a mesh with the same resolution of 1*B* and 1*B*-1*T* grids, that was introduced in the study of Horcas et al. (2016b). The computational factor associated to the presented *Full machine rigid*, that used the NLH approach, was found to be only the 3.8% of the value expected for *Full machine rigid-URANS*. The comparison of *Full machine rigid* and *Full machine flexible* simulations revealed an overhead associated to the modeling of the rotor aeroelasticity of 35%.

5. Conclusions and future work

In this paper, the development of a *2-way coupling* FSI methodology for the study of horizontal axis wind turbines dynamic aeroelasticity was presented. The solution of the unsteady Navier–Stokes flow equations relied on the NLH method. The

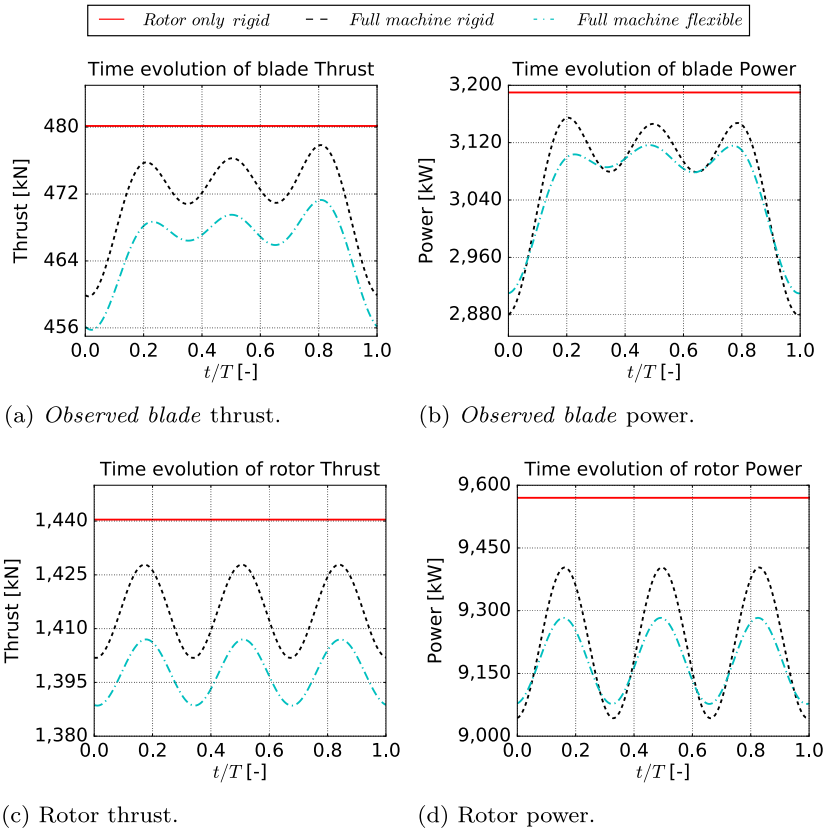

(a) *Observed blade* thrust. (b) *Observed blade* power.

(c) Rotor thrust. (d) Rotor power.

Fig. 22. Time reconstruction of DTU 10 MW RWT loads for *Full machine rigid* and *Full machine flexible* simulations. The corresponding values of the *Rotor only rigid* computation were also included.

Table 7
Time-averaged value and amplitude of oscillation of DTU 10 MW RWT rotor loads for all the performed computations.

	Time-averaged			Amplitude of oscillation		
	Rotor only rigid	*Full machine rigid*	*Full machine flexible*	*Rotor only rigid*	*Full machine rigid*	*Full machine flexible*
Rotor thrust [kN]	1,440.4	1,414.8	1,397.8	–	13.01	9.24
Thrust coefficient [-]	0.872	0.856	0.846	–	0.008	0.006
Rotor power [kW]	9,570.0	9,223.1	9,180.0	–	180.3	103.0
Power coefficient [-]	0.552	0.532	0.529	–	0.010	0.006

Table 8
Summary of the computational resources employed for the DTU 10 MW RWT simulations.

	Rotor only rigid	*Full machine rigid*	*Full machine rigid-URANS*[a]	*Full machine flexible*
Computational method	RANS	NLH	URANS	NLH
Millions of mesh nodes (N_n)	7	13	25	13
#Processors (N_p)	8	64	128	64
Computational time in hours (T_h)	8	49	∼1,250	66
Computational factor ($\frac{T_h N_p}{N_n}$)	9	241	∼6,400	325

[a] The computational cost was estimated based on a mesh presented in Horcas et al. (2016b), suitable for URANS method simulations.

structure was linearized based on a set of mode shapes and natural frequencies. The aeroelastic equilibrium was ensured through a set of equations linking the structural displacements and the fluid loads for both the time-averaged and the harmonic contributions. Computed structural deflections were diffused into the whole CFD domain by means of the harmonic adaptation of a state-of-the-art mesh deformation method. A general NLH formulation was adopted for the fluid and structure coupling in the frequency domain, allowing the use of the presented development in a wide range of applications.

The performance of the presented methodology was first assessed in an academic test case: a 2D cylinder undergoing laminar vortex shedding. In the first stage of this analysis, the cylinder was assumed to be fixed. In order to identify the natural shedding frequency of the flow with the NLH method, an iterative *phase error* technique was employed. Reasonably

good predictions of the *Strouhal number* were found, with maximum underestimations of 7% when compared to available experimental results. These discrepancies were assumed to be related to the numerical model parameters. In particular, both the influence of the size of the domain and the mesh refinement of the downstream block could be assessed in future studies. The cylinder loads predicted by the NLH method also matched the trend established by the experimental data. In the second step of this academic study the cylinder was enabled to oscillate elastically in the transversal direction of the flow due to the action of the unsteady fluid loading. The resulting set-up is known in the literature as the VIV of a cylinder in transversal oscillation. Several simulations based on the presented *2-way coupling* FSI methodology were performed, aiming to evaluate the combined impact of the spring frequency and the associated damping ratio in the so-called *lock-in region*. As for the fixed cylinder configuration, the identification of the aeroelastic frequency of the system required of an initial iterative procedure. The results issued from this work were compared with other authors' simulations. The evolution of the predicted amplitudes of oscillation and the computed cylinder loads showed a reasonable agreement with respect to these numerical references. However small discrepancies were observed, probably related to the effects of the *Reynolds number* and to potential errors in the prediction of the shedding frequency.

The developed *2-way coupling* FSI methodology was then used in order to study the dynamic aeroelasticity of the complete DTU 10 MW RWT wind turbine assembly. For this application the main source of unsteadiness could be related to passage of the blades in front of the tower. Hence, the fundamental harmonics of the simulation were determined by the rotor frequency through the concept of BPF. A nominal operating point was studied, and the rotor flexibility was considered through a linearized model of the blade structure. A time-averaged blade tip deflection parallel to the rotor axis of 9.15%R was predicted, implying a margin of 54.3% with regards to the DTU 10 MW RWT tower clearance. The blade deflection transients exhibited a decay in the vicinity of the tower position, with peak-to-peak amplitudes representing less than 4% of the corresponding time-averaged values. The results of this coupled simulation concerning the blade and rotor loading were compared with two additional computations, both assuming *rigid* blades, that modeled the isolated DTU 10 MW RWT rotor and the complete machine. When compared to the isolated *rigid* rotor reference, the complete machine computations observed a decrease of the time-averaged loads. This reduction was more important for the *2-way coupling* FSI simulation due to the effects of the rotor aeroelasticity. In particular, the time-averaged rotor thrust decrease was multiplied by 1.7, while the analogous factor for the time-averaged power was 1.1. In addition, the blade aeroelasticity was found to reduce the rotor loads fluctuation. When compared to the *rigid* full machine simulation, the *2-way coupling* FSI computation observed attenuation factors of 0.7 for the rotor thrust and 0.6 for the rotor power oscillations.

Two main contributions can be extracted from this paper. On the one hand, it constitutes a first experience in assessing the performance of the NLH method when modeling the vortex shedding. It was shown that the uncertainty in the value of the shedding frequency can be bypassed by the application of an iterative simulation process. Even if this approach has several limitations from the industrialization point of view, it opens the door to a potential development concerning the automatic shedding frequency identification. On the other hand, the first application of a non-linear frequency CFD method for the study of the dynamic aeroelasticity of a complete wind turbine was presented. The developed methodology was found to be one order of magnitude faster than a state-of-the-art time marching approach. The paper also includes a comprehensive analysis of aeroelastic effects of the DTU 10 MW RWT due to the presence of the tower, that can be used by other authors for benchmarking purposes. However, the accuracy of the proposed technique should be validated against representative experimental data when available.

Future work will be devoted to extend the set of performed simulations. For the case of the 2D cylinder undergoing VIV, additional configurations should be considered in order to assess the performance of the developed methodology in the capture of the maximum oscillation amplitude. Regarding the DTU 10 MW RWT it could be interesting to analyze a load case out of the nominal operation, such as a gust response, where the aeroelasticity effects are expected to be more pronounced. The influence of the incoming flow and rotor axis misalignment, due to the tilt angle, could be also considered in the NLH-based simulations by means of an inlet perturbation. Additionally the presented aeroelastic coupling could be improved in terms of modeling capabilities by including the gravitational loads, and in terms of convergence by accounting for the aerodynamic Jacobian in the update of the generalized displacements (as performed by Bernardini et al., 2013). Finally, the sensibility of the presented methodology could be evaluated by increasing the number of solved harmonics, in order to account for the local effects of DTU 10 MW RWT vortex shedding at low span.

Acknowledgments

The authors acknowledge the European Commission for their research grant under the project FP7-PEOPLE-2012-ITN 309395 *Mare — Wint* (new MAterials and REliability in offshore WINd Turbines technology), as well as all the members from the FINE™/Turbo team of NUMECA International for their valuable and active contribution.

References

Adhikari, S., 2000. Damping Models for Structural Vibration (Ph.D. thesis). Cambridge University, p. 228.

Anagnostopoulos, P., Bearman, P., 1992. Response characteristics of a vortex-excited cylinder at low reynolds numbers. J. Fluids Struct. 6 (1), 39–50. http://dx.doi.org/10.1016/0889-9746(92)90054-7.

Aranake, A.C., 2013. Computational analysis of shrouded wind turbine configurations. In: 51st AIAA Aerospace Sciences Meeting Including the New Horizons Forum and Aerospace Exposition, Grapevine.

Bak, C., Zahle, F., Bitsche, R., Kim, T., Yde, A., Henriksen, L.C., Natajaran, A., Hansen, M.H., 2013. Description of the DTU 10 MW Reference Wind Turbine. Technical Report Technical University of Denmark Wind Energy; Roskilde, Denmark, p. 138.

Bernardini, G., Serafini, J., Molica Colella, M., Gennaretti, M., 2013. Analysis of a structural-aerodynamic fully-coupled formulation for aeroelastic response of rotorcraft. Aerosp. Sci. Technol. 29 (1), 175–184. http://dx.doi.org/10.1016/j.ast.2013.03.002.

Besem, F.M., 2015. Aeroelastic Instabilities due to Unsteady Aerodynamics (Ph.D. thesis). Duke University.

Bielawa, R.L., 1992. In: Przemieniecki, J.S. (Ed.), Rotatory Wind Structural Dynamics and Aeroelasticity. American Institute of Aeronautics and Astronautics, Wasignton, DC, p. 363.

Campobasso, S., Gigante, F., Drofelnik, J., 2014a. Turbulent unsteady flow analysis of horizontal axis wind turbine airfoil aerodynamics based on the harmonic balance Reynolds-Averaged Navier-Stokes equations. In: ASME Turbo Expo 2014: Turbine Technical Conference and Exposition. The American Society of Mechanical Engineers, Düsseldrof, Germany. http://dx.doi.org/10.1115/GT2014-25559.

Campobasso, S., Yan, M., Drofelnik, J., Piskopakis, A., Caboni, M., 2014b. Compressible Reynolds-Averaged Navier-Stokes analysis of wind turbine turbulent flows using a Fully-Coupled Low-Speed preconditioned multigrid solver. In: ASME Turbo Expo 2014. The American Society of Mechanical Engineers, Düsseldrof, Germany. http://dx.doi.org/10.1115/GT2014-25562.

Carrión, M., 2014. Low Mach Number CFD for Wind Turbine Analysis (Ph.D. thesis). University of Liverpool.

Corson, D., Griffith, D.T., Ashwill, T., Shakib, F., 2012. Investigating aeroelastic performance of multi-mega watt wind turbine rotors using CFD. In: 53rd AIAA/ASME/ASCE/AHS/ASC Structures, Structural Dynamics and Materials Conference. In: Structures, Structural Dynamics, and Materials and Co-located Conferences, American Institute of Aeronautics and Astronautics, http://dx.doi.org/10.2514/6.2012-1827.

Debrabandere, F., 2014. Computational Methods for Industrial Fluid-Structure Interactions (Ph.D. thesis). Université de Mons (UMONS).

Dowell, E.H., Hall, K.C., Thomas, J.P., Kielb, R.E., Spiker, M.A., Denegri Jr., C.M., 2008. A new solution method for unsteady flows around oscillating bluff bodies. In: IUTAM Symposium on Fluid-Structure Interaction in Ocean Engineering. Springer, pp. 37–44.

Elfarra, M.A., Sezer-Uzol, N., Akmandor, I.S., 2014. NREL VI rotor blade: numerical investigation and winglet design and optimization using CFD. Wind Energy 17 (4), 605–626. http://dx.doi.org/10.1002/we.1593.

Fan, Z., Kang, S., 2009. Numerical simulation of the aerodynamic performance of HAWT. In: EWEC 2009, Marseille, France: European Wind Energy Association, pp. 1–7.

Fey, U., König, M., Eckelmann, H., 1998. A new Strouhal-Reynolds-number relationship for the circular cylinder in the range $47 < \mathrm{Re} < 2 \times 10^5$. Phys. Fluids 10 (7), 1547. http://dx.doi.org/10.1063/1.869675.

Glauert, H., 1935. Aerodynamic Theory: A General Review of Progress Under a Grant of the Guggenheim Fund for the Promotion of Aeronautics. Springer Berlin Heidelberg, Berlin, Heidelberg, pp. 196–360. http://dx.doi.org/10.1007/978-3-642-91487-4. (Chapter) Airplane P..

Griffin, O., Skop, R., Koopmann, G., 1973. The vortex-excited resonant vibrations of circular cylinders. J. Sound Vib. 31 (2), 235–249. http://dx.doi.org/10.1016/S0022-460X(73)80377-3.

Hakimi, N., 1997. Preconditioning methods for time dependent Navier-Stokes equations. Application to Environmental and Low Speed Flows (Ph.D. thesis). Vrije Universiteit Brussel, pp. 1–162.

Hall, K.C., Thomas, J.P., Clark, W.S., 2002. Computation of unsteady nonlinear flows in cascades using a harmonic balance technique. AIAA J. 40 (5), 879–886. http://dx.doi.org/10.2514/2.1754.

Hansen, M.O.L., Sørensen, J.N., Voutsinas, S., Sørensen, N.N., Madsen, H.A., 2006. State of the art in wind turbine aerodynamics and aeroelasticity. Prog. Aerosp. Sci. 42 (4), 285–330. http://dx.doi.org/10.1016/j.paerosci.2006.10.002.

He, L., Ning, W., 1998. Efficient approach for analysis of unsteady viscous flows in turbomachines. AIAA J. 36 (11), 2005–2012. http://dx.doi.org/10.2514/2.328.

Heinz, J.C., Sørensen, N.N., Zahle, F., 2016. Fluid-structure interaction computations for geometrically resolved rotor simulations using CFD. Wind Energy 17. http://dx.doi.org/10.100/we.1976.

Hirsch, C., 1990. Numerical Computation of Internal and External Flows, Volume 2, Computational Methods for Inviscid and Viscous Flows, first ed.. Wiley-Interscience, John Wiley & Sons, Ltd, pp. 1–691.

Hoerner, S.F., 1965. Fluid-Dynamic Drag, Practical Information on Aerodynamic Drag and Hydrodynamic Resistance. Hoerner Fluid Dynamics, Washington D.C, p. 455.

Holierhoek, J.G., 2008. Aeroelasticity of Large Wind Turbines (Ph.D. thesis). Technical University of Delft, p. 360, ISBN 9789090236278.

Horcas, S.G., Debrabandere, F., Tartinville, B., Hirsch, C., Coussement, G., 2015. Hybrid mesh deformation tool for offshore wind turbines aeroelasticity prediction. In: Ferrer, E., Montlaur, A. (Eds.), CFD for Wind and Tidal Offshore Turbines SE - 8. In: Springer Tracts in Mechanical Engineering, Springer International Publishing, pp. 83–94. http://dx.doi.org/10.1007/978-3-319-16202-7_8.

Horcas, S.G., Debrabandere, F., Tartinville, B., Hirsch, C., Coussement, G., 2016. CFD study of DTU 10 MW RWT aeroelasticity and rotor-tower interactions, In: Ostachowicz, W., McGugan, M., Schroder-Hinrichs, J.-U., Luczac, M. (Eds.), MARE-WINT, New Materials and Reliability in Offshore WInd Turbine Technology. first ed.. Springer International Publishing, pp. 309–334. http://dx.doi.org/10.1007/978-3-319-39095-6_18. (Chapter 18).

Horcas, S.G., Debrabandere, F., Tartinville, B., Hirsch, C., Coussement, G., 2016. Rotor-tower interactions of DTU 10MW reference wind turbine with a non-linear harmonic method. Wind Energy 20, 619–636. http://dx.doi.org/10.1002/we.2027.

Howison, J.C., 2015. Aeroelastic Analysis of a Wind Turbine Blade Using the Harmonic Balance Method (Ph.D. thesis). University of Tennessee.

Howison, J., Ekici, K., 2014. Dynamic stall analysis using harmonic balance and correlation-based $\gamma - \overline{Re_{\theta t}}$ transition models for wind turbine. Wind Energy. http://dx.doi.org/10.1002/we.1803.

Howison, J.C., Thomas, J., Ekici, K., 2015. Progress on a wind turbine aeroelastic solution methodology using harmonic balance. In: 33rd Wind Energy Symposium. American Institute of Aeronautics and Astronautics, Kissimmee, Florida.

Hsu, M.-C., Bazilevs, Y., 2012. Fluid-structure interaction modeling of wind turbines: simulating the full machine. Comput. Mech. 50 (6), 821–833. http://dx.doi.org/10.1007/s00466-012-0772-0.

Jameson, A., Schmidt, W., Turkel, E., 1981. Numerical solutions of the Euler equations by finite volume methods using Runge-Kutta time-stepping schemes. AIAA Paper, pp. 1–19 http://dx.doi.org/10.2514/6.1981-1259, ISBN 9781441976314.

Jonkman, J., Butterfield, S., Musial, W., Scott, G., 2009. Definition of a 5-MW reference wind turbine for offshore system development. Technical Report NREL/TP-500-38060 National Renewable Energy Laboratory (NREL), Golden, CO.

Jonkman, J., Musial, W., 2010. Offshore Code Comparison Collaboration (OC3) for IEA Task 23 Offshore Wind Technology and Deployment. Technical Report NREL/TP-5000-48191 National Renewable Energy Laboratory (NREL).

Jonkman, J., Robertson, A., Popko, W., Vorpahl, F., Zuga, A., Kohlmeier, M., Larsen, T., Yde, A., Saetertro, K., Osktad, K.M., Nichols, J., Nygaard, T.A., Gao, Z., Manolas, D., KIm, K., Yu, Q., Shi, W., Park, H., Vasquez-Rojas, A., Dubois, J., Kaufer, D., Thomassen, P., de Ruiter, M.J., Peeringa, J.M., Zhiwen, H., von Waaden, H., 2012. Offshore Code Comparison Collaboration Continuation (OC4), Phase I - Results of Coupled Simulations of an Offshore Wind Turbine with Jacket Support Structure. Technical Report NREL/CP-5000-54124 National Renewable Energy Laboratory (NREL).

Liu, L., Dowell, E.H., Thomas, J., 2005. Higher order harmonic balance analysis for limit cycle oscillations in an airfoil with cubic restoring forces. In: 46th AIAA/ASME/ASCE/AHS/ASC Structures, Structural Dynamics and Materials Conference, April, pp. 1–10 http://dx.doi.org/10.2514/6.2005-1918, ISSN 02734508, ISBN 978-1-62410-065-9.

McMullen, M.S., 2003. The Application of Non-linear Frequency Domain Methods to the Euler and Navier-Stokes Equations (Ph.D. thesis). Standford University.
Norberg, C., 2001. Flow around a circular cylinder: Aspects of fluctuating lift. J. Fluids Struct. 4 (15), 459–469. http://dx.doi.org/10.1006/jfls.2000.0367.
NUMECA International, 2016a. Autogrid5™ v10.2 User Manual.
NUMECA International, 2016b. FINE™/Turbo v10.2 User Manual.
Owens, B.C., Griffith, D.T., Resor, B.R., Hurtado, J.E., 2013. Impact of modeling approach on flutter predictions for very large wind turbine blade designs. In: AHS 69th Annual Forum. American Helicopter Society, Phoenix, Arizona.
Placzek, A., Sigrist, J.F., Hamdouni, A., 2009. Numerical simulation of an oscillating cylinder in a cross-flow at low Reynolds number: Forced and free oscillations. Comput. & Fluids 38 (1), 80–100. http://dx.doi.org/10.1016/j.compfluid.2008.01.007.
Robertson, A., Jonkman, J., Musial, W., Vorpahl, F., Popko, W., 2013. Offshore Code Comparison Collaboration, Continuation : Phase II results of a floating semisubmersible wind system. Technical Report NREL/CP-5000-60600 National Renewable Energy Laboratory (NREL).
Robertson, A., Wendt, F., Jonkman, J., Popko, W., Vorpahl, F., Trygve, C., Bachynski, E.E., Bayati, I., Beyer, F., Vaal, J.B.D., Harries, R., Yamaguchi, A., Kim, B., Zee, T.V.D., Bozonnet, P., Aguilo, B., Bergua, R., Qvist, J., Qijun, W., Chen, X., Guerinel, M., Tu, Y., Yutong, H., Li, R., Bouy, L., 2015. OC5 Project Phase I : Validation of Hydrodynamic Loading on a Fixed Cylinder. Technical Report NREL/CP-5000-63567 National Renewable Energy Laboratory (NREL).
Schepers, J.G., Snel, H., 2007. Model Experiments in Controlled Conditions, Final Report. Technical Report Energy research Centre of the Netherlands (ECN).
Shiels, D., Leonard, A., Roshko, A., 2001. Flow-induced vibration of a circular cylinder at limiting structural parameters. J. Fluids Struct. 15 (1), 3–21. http://dx.doi.org/10.1006/jfls.2000.0330.
Simulia, D.S.C., 2008. Abaqus Analysis version 6.8 User's Manual.
Spalart, P., Allmaras, S., 1992. A one-equation turbulence model for aerodynamic flows. In: 30th Aerospace Sciences Meeting and Exhibit. In: Aerospace Sciences Meetings, American Institute of Aeronautics and Astronautics, pp. 1–22.
Spiker, M.A., Kielb, R.E., Thomas, J.P., Hall, K.C., 2009. Application of enforced motion to study 2-D cascade lock-in effect. In: 47th AIAA Aerospace Sciences Meeting Including the New Horizons Forum and Aerospace Exposition. American Institute of Aeronautics and Astronautics, Orlando, Florida.
Spiker, M.A., Thomas, J.P., Hall, K.C., Kielb, R.E., Dowell, E.H., 2006. Modeling cylinder flow vortex shedding with enforced motion using a harmonic balance approach. In: 47th AIAA/ASME/ASCE/AHS/ASC Structures, Structural Dynamics, and Materials Conference. American Institute of Aeronautics and Astronautics, Newport, Rhode Island, . http://dx.doi.org/10.2514/6.2006-1965. May.
Suárez, J.M., Doerffer, P., 2015. CFD validated technique for prediction of aerodynamic characteristics on horizontal axis wind energy turbines. In: EWEA Offshore 2015, Copenhagen, pp. 1–10.
Suárez, J.M., Doerffer, P., Szulc, O., Tejero, F., 2015. Aerodynamic analysis of wind turbine rotor blades. Task Q. 19 (2), 129–140.
Thomas, J.P., Dowell, E.H., Hall, K.C., 2002. Nonlinear inviscid aerodynamic effects on transonic divergence, flutter, and limit-cycle oscillations. AIAA J. 40 (4), 638–646. http://dx.doi.org/10.2514/3.15109.
Thomas, J., Dowell, E.H., Hall, K., Denegri, C., 2004. Modeling limit cycle oscillation behavior of the F-16 fighter using a harmonic balance approach. In: 45th AIAA/ASME/ASCE/AHS/ASC Structures, Structural Dynamics & Materials Conference, April http://dx.doi.org/10.2514/6.2004-1696 ISSN 02734508, ISBN 978-1-62410-079-6.
Thomas, J., Dowell, E.H., Hall, K., Denegri, C., 2005. Further investigation of modeling limit cycle oscillation behavior of the F-16 Fighter using a harmonic balance approach. Amer. Inst. Aeronaut. Astronaut. J.. http://dx.doi.org/10.2514/6.2004-1696.
Uyttersprot, L., 2014. Inverse Distance Weighting Mesh Deformation. A Robust and Efficient Method for Unstructured Meshes. Technical Report TU Delft Delft.
Velazquez, A., Swartz, R.A., 2012. Gyroscopic effects of horizontal axis wind turbines using stochastic aeroelasticity via spinning finite elements. In: ASME 2012 Conference on Smart Materials, Adaptive Structures and Intelligent Systems. American Society of Mechanical Engineers (ASME), Stone Mountain, Georgia.
Vilmin, S., Lorrain, E., Hirsch, C., Swoboda, M., 2006. Unsteady flow modeling across the rotor/stator interface using the nonlinear harmonic method. In: ASME Turbo Expo 2006, Barcelona, pp. 1–11 http://dx.doi.org/10.1115/GT2006-90210, ISBN 0-7918-4241-X.
Wieselberger, C., 1921. Neuere feststellungen Über die gesetze des Flüssigkeits luftwiderstands. Physik Z 22, 321–328.
Williamson, C., 1996. Vortex dynamics in the cylinder wake. Annu. Rev. Fluid Mech. 28, 477–539.
Yelmule, M., Anjuri, E., 2013. CFD predictions of NREL Phase VI rotor experiments in NASA/AMES Wind tunnel. Int. J. Renewable Energy Res. 3 (2), 261–270.
Yu, D.O., Kwon, O.J., 2014. Predicting wind turbine blade loads and aeroelastic response using a coupled CFD-CSD method. Renewable Energy 70, 184–196. http://dx.doi.org/10.1016/j.renene.2014.03.033.